

Field measurements demonstrate distinct initiation and cessation thresholds governing aeolian sediment transport flux

Raleigh L. Martin*, Department of Atmospheric and Oceanic Sciences, University of California, Los Angeles, CA 90095

Jasper F. Kok, Department of Atmospheric and Oceanic Sciences, University of California, Los Angeles, CA 90095

Key Points

1. We provide the first field-based evidence for separate fluid and impact thresholds in aeolian saltation
2. Saltation occurrence is mediated by both thresholds, but fluid (impact) threshold dominates during infrequent (near-continuous) transport
3. Both thresholds are important for high-frequency saltation prediction, but long-term aeolian fluxes are governed mostly by impact threshold

*raleighm@atmos.ucla.edu

Abstract

Wind-blown sand and dust models depend sensitively on the threshold wind stress. However, laboratory and numerical experiments suggest the coexistence of distinct “fluid” and “impact” thresholds for the initiation and cessation of aeolian saltation, respectively. Because aeolian models typically use a single threshold, existence of dual thresholds complicates the prediction of wind-driven transport. Here, we derive the first field-based estimates of distinct fluid and impact thresholds from high-frequency saltation measurements at three field sites, and we determine how these thresholds control the occurrence of saltation. We show that, when saltation is mostly inactive, its instantaneous occurrence is governed primarily by wind exceedance of the fluid threshold. As saltation activity increases, so too does the relative importance of the impact threshold, until it dominates under near-continuous transport conditions. Although both thresholds are thus important for high-frequency saltation prediction, we find that the time-averaged saltation flux is primarily governed by impact threshold.

1. Introduction

Determining the threshold wind shear stress for the occurrence of wind-driven (“aeolian”) sand transport has been a central challenge for studies of planetary, coastal, and desert aeolian processes [e.g., *Bagnold*, 1941; *Iversen and White*, 1982; *Shao and Lu*, 2000]. In desert and semi-arid environments, the aeolian saltation threshold regulates the frequency of topsoil erosion and mineral dust emission [e.g., *Rice et al.*, 1999]. Where sand dunes and ripples are present, the saltation threshold governs the frequency of migration of these bedforms [e.g., *Fryberger et al.*, 1979]. Aeolian transport studies indicate that sand flux scales linearly [e.g., *Martin and Kok*, 2017] or to the 3/2 power [e.g., *Bagnold*, 1941] of wind stress in excess of the saltation threshold, so slight shifts in the presumed threshold value can profoundly change predictions of the total sand saltation flux and associated dust emissions [e.g., *Sherman et al.*, 2013; *Kok et al.*,

2014; *Webb et al.*, 2016]. Uncertainty in threshold is therefore a major issue for studies relating aeolian transport observations to atmospheric conditions on Earth [e.g., *Lindhorst and Betzler*, 2016], Mars [e.g., *Bridges et al.*, 2012; *Ayoub et al.*, 2014] and other planetary surfaces [e.g., *Lorenz and Zimbelman*, 2014].

Despite the central importance of the saltation threshold in predicting sand and dust fluxes, there remains a lack of agreement over the best way to model or even measure this threshold [*Barchyn and Hugenholtz*, 2011]. Predictive equations for saltation (and the resulting dust emission) usually include a single threshold value [*Barchyn et al.*, 2014b], traditionally the “fluid threshold” shear stress τ_{ft} for initiating saltation transport solely by aerodynamic forces [*Bagnold*, 1941; *Iversen and White*, 1982; *Marticorena and Bergametti*, 1995]. However, theory and measurements suggest the presence of a separate, lower “impact threshold” shear stress τ_{it} required to sustain saltation through saltator impacts with the soil bed. This impact threshold has been hypothesized to equal the rate of momentum dissipation at the surface [*Owen*, 1964], which is controversial [*Kok et al.*, 2012], but for which there is now limited experimental support [*Walter et al.*, 2014].

Based on the role of the impact threshold in the steady-state saltation momentum balance, most recent saltation models use impact threshold alone as the zero-intercept value for the saltation flux law [*Ungar and Haff*, 1987; *Creyssels et al.*, 2009; *Martin and Kok*, 2017]. However, recent studies have argued for the need to simulate the path-dependence of saltation flux responses to turbulent wind fluctuations around both impact and fluid thresholds [*Kok*, 2010a, 2010b]. The ratio of impact and fluid thresholds governing this hysteresis depends primarily on the particle-fluid density ratio, which determines the relative contributions of particle impacts and direct fluid lifting to particle entrainment [*Kok*, 2010b; *Pähzt and Durán*, 2016]. On Earth, the experimentally [*Bagnold*, 1937] and numerically [*Kok*, 2010b] predicted ratio of impact and fluid threshold shear velocities u_{*it}/u_{*ft} is approximately 0.82, whereas u_{*it}/u_{*ft} is predicted to be as low as 0.1 on Mars [*Kok*, 2010a].

Though numerical and experimental studies predict fluid and impact thresholds, field studies have not yet confirmed the existence of these two separate thresholds, let alone determined which should be used for modeling sand and dust flux. Field-based determinations of fluid and impact threshold have been hindered by the generally poor correlation between time series of wind speed and saltation flux at short time scales [e.g., *Wiggs et al.*, 2004; *Davidson-Arnott et al.*, 2005; *Davidson-Arnott and Bauer*, 2009], due to spatial separation between saltation and wind measurements [*Baas*, 2008], variability in surface grain configurations [*Nickling*, 1988; *Li et al.*, 2008], and fluctuations in the turbulent winds driving saltation [*Carneiro et al.*, 2015].

Here, we use comprehensive high-frequency field measurements of aeolian transport at three field sites to determine which threshold(s) should be used in models for sand and dust flux. In Section 2, we present theory for relating fluid and impact thresholds, wind speed fluctuations, and saltation transport occurrence. In Section 3, we describe methods for applying this theory to estimate thresholds from field data. In Section 4, we present the first field-based estimates of separate fluid and impact thresholds, and we examine how well these thresholds predict measured saltation activities. In Section 5, we discuss the role of fluid and impact thresholds in modeling sand and dust fluxes. We make concluding remarks in Section 6.

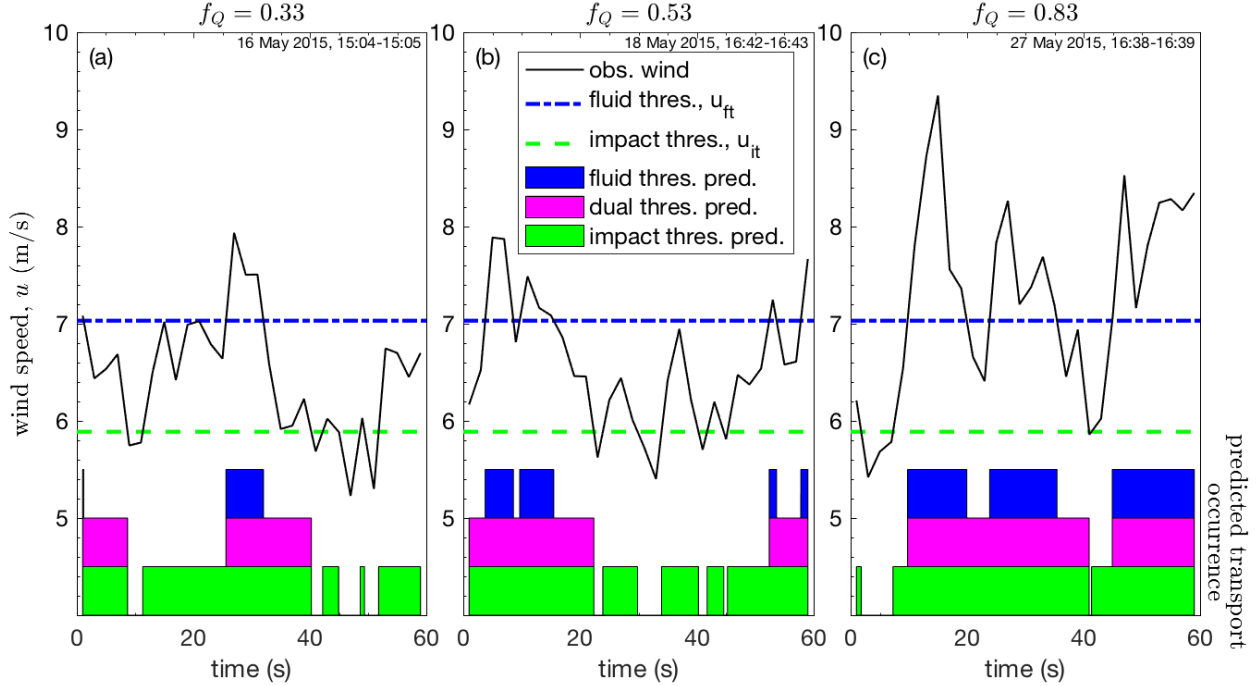


Figure 1. Illustration of variations in wind speed u and predicted transport occurrence for time intervals with (a) low ($f_Q = 0.33$), (b) medium ($f_Q = 0.53$), and (c) high ($f_Q = 0.83$) observed transport activity at Oceano. Blue and green dashed lines indicate respective fluid and impact threshold wind speeds, u_{ft} and u_{it} . Based on fluctuations in u with respect to u_{ft} and u_{it} , we predict expected occurrence of saltation transport governed by the fluid threshold alone (Eq. 1 – shown as solid blue bars near bottom of each panel), the impact threshold alone (Eq. 2 – green bars), and by dual thresholds acting together (Eq. 3 – magenta bars). Due to the spatial separation between instruments measuring wind and saltation, we do not expect a direct correspondence between particular instances of predicted and measured saltation occurrence. We thus instead analyze the statistics of transport occurrence portrayed by observed saltation activities f_Q over full $\Delta t = 1$ minute analysis intervals, in comparison to activity predictions by fluid ($f_{Q,ft}$), impact ($f_{Q,it}$), and dual ($f_{Q,dual}$) threshold control, here: (a) 0.13, 0.80, 0.37; (b) 0.23, 0.83, 0.50; and (c) 0.63, 0.87, 0.77.

2. Theory

We expect the occurrence of aeolian saltation transport to be governed by both the fluid and impact thresholds, based on the relative importance of transport initiation versus cessation. In this section, we describe how, over time intervals of intermittent saltation that include many threshold crossings, the combined contributions of τ_{ft} and τ_{it} should produce an intermediate “effective” threshold stress τ_{th} that varies systematically with the fraction of time f_Q that saltation is active.

2.1. Regulation of saltation occurrence by fluid and impact thresholds

Consider time series of near-surface horizontal wind speed $u(t)$ relative to fluid and impact threshold wind speeds, u_{ft} and u_{it} respectively, corresponding to τ_{ft} and τ_{it} (Fig. 1). When $u \geq$

u_{ft} , we expect the occurrence of saltation transport; conversely, when $u < u_{it}$, transport should not occur. Ambiguity in prediction of saltation occurrence arises in cases where $u_{it} \leq u < u_{ft}$.

There are three possible ways to address this ambiguity. First, fluid threshold could dominate:

$$f_{Q,ft} = f_+, \quad (1)$$

where $f_{Q,ft}$ is the expected fraction of time with active saltation by fluid threshold control, and f_+ is the fraction of time with $u \geq u_{ft}$. Second, impact threshold could dominate:

$$f_{Q,it} = f_+ + f_\sim, \quad (2)$$

where $f_{Q,it}$ is the expected transport activity by impact threshold control, and f_\sim is the fraction of time with $u_{it} \leq u < u_{ft}$. Third, dual thresholds could together control saltation activity in a path-dependent manner [Kok, 2010b]:

$$f_{Q,dual} = f_+ + f_\downarrow f_\sim, \quad (3)$$

where $f_{Q,dual}$ is the expected transport activity for dual threshold control, and f_\downarrow is the fraction of time within $u_{it} \leq u < u_{ft}$ for which the most recent threshold crossing was a downward crossing of u_{ft} .

To illustrate these different threshold control scenarios, Fig. 1 displays three sample time series of wind speed straddling fluid and impact thresholds and corresponding predictions for the occurrence of saltation transport. (Methods for obtaining $u(t)$, u_{ft} , and u_{it} will be described in further detail below.) By definition, saltation is expected to occur least frequently for fluid threshold control (Eq. 1) most frequently for impact threshold control (Eq. 2), and somewhere in between for dual threshold control (Eq. 3), i.e., $f_{Q,ft} \leq f_{Q,dual} \leq f_{Q,it}$.

Over time intervals of intermittent saltation, the relative proximity of $f_{Q,dual}$ to $f_{Q,ft}$ and $f_{Q,it}$ should depend on the relative occurrence of intermediate wind speeds ($u_{it} \leq u < u_{ft}$) originating from above u_{ft} versus from below u_{it} . In Fig. 1a, most intermediate winds originate from $u \leq u_{it}$ and a state of expected non-transport (i.e., $f_\downarrow \rightarrow 0$); therefore, $f_{Q,dual}$ is closer to $f_{Q,ft}$, indicating that fluid threshold mostly controls saltation occurrence. Conversely, in Fig. 1c, most intermediate winds originate from $u > u_{ft}$ and a state of expected transport (i.e., $f_\downarrow \rightarrow 1$); therefore, $f_{Q,dual}$ is closer to $f_{Q,it}$, indicating that now impact threshold mostly controls saltation occurrence. In cases of intermediate winds approached from both directions (i.e., $f_\downarrow \approx 0.5$) and states of both non-transport and transport, $f_{Q,dual}$ is roughly halfway between $f_{Q,ft}$ and $f_{Q,it}$ (Fig. 1b).

2.2. “Effective” threshold in relation to dual thresholds and transport activity

To quantify the relative contributions of fluid and impact thresholds to the occurrence of saltation, we adopt a statistical definition of “effective” threshold u_{th} based on the “Time Frequency Equivalence Method” [Stout and Zobeck, 1997; Stout, 2004; Wiggs *et al.*, 2004]:

$$u_{th} = \Phi_u(1 - f_Q), \quad (4)$$

where $\Phi_u(1 - f_Q)$ is the value in the cumulative distribution of wind speeds Φ_u corresponding to the time fraction of inactive saltation, $1 - f_Q$. Thus, Eq. 4 asserts a statistical equivalence between the fraction of winds above u_{th} and the fraction of time with active saltation f_Q .

By definition, effective threshold u_{th} does not describe the threshold wind speed for individual instances of saltation initiation or cessation; rather, it describes the combined effect of both impact and fluid thresholds on saltation activity f_Q for time intervals of intermittent saltation. In particular, by the dual-threshold hypothesis (Eq. 3), both u_{it} and u_{ft} should contribute to f_Q , such that $u_{it} \leq u_{th} < u_{ft}$. Based on our reasoning for Fig. 1, we further hypothesize that cases of mostly inactive transport (i.e., $f_Q \approx 0$) should produce fluid threshold dominance (Eq. 1), whereas cases of mostly active transport (i.e. $f_Q \approx 1$) should produce impact threshold dominance (Eq. 2). Between these limiting cases, the effective threshold should vary with transport activity such that:

$$\tau_{th} = f_Q \tau_{it} + (1 - f_Q) \tau_{ft}, \quad (5)$$

where τ_{th} is the equivalent effective threshold shear stress for u_{th} . This phenomenon of decreasing τ_{th} with increasing wind speed (and presumably f_Q) was indeed observed in numerical simulations by Schönfeldt [2004]. If correct, Eq. 5 offers a way to estimate impact and fluid thresholds from measurements of effective threshold and saltation activity.

Below, in Section 3, we describe methods to estimate effective thresholds and saltation activities from field data. Then, in Section 4, we estimate impact and fluid thresholds from Eq. 5 and compare measured saltation activities against our hypotheses for saltation occurrence controlled by fluid, impact, and dual thresholds (Eqs. 1-3).

3. Methods

We analyzed simultaneous high-frequency measurements of active saltation and wind at three field sites (Jericoacoara, Rancho Guadalupe, and Oceano) with distinctive soil conditions. Multiple (3-9) Wenglor optical sensors [Barchyn *et al.*, 2014a] at heights from the bed surface up to ≈ 0.3 m counted saltating particles (25 Hz), which we converted to vertically-integrated saltation particle counts rates N (Fig. 2a). A sonic anemometer at height $z_U \approx 0.5$ m measured wind velocity (25 Hz at Jericoacoara and Rancho Guadalupe, 50 Hz at Oceano) (Fig. 2d). Though our field deployments (described further in Martin *et al.* [2017]) included anemometers at multiple heights, we chose to use measurements from only the lowest anemometer (i.e., $z_U \approx 0.5$ m) at each site, because we expected these measurements to be most representative of wind fluctuations at the sand surface.

To calculate saltation activity f_Q and effective threshold wind speed u_{th} , we applied $\delta t = 2$ s interval averaging to saltation (Fig. 2b) and wind (Fig. 2e) time series, then we subdivided these data into $\Delta t = 1$ minute analysis intervals. Within each analysis interval, we calculated saltation activity f_Q as the fraction of δt increments within Δt for which N was nonzero (Fig 2c) and applied a correction (see Supporting Information Text S1) to account for the possibility of false negatives. For each Δt , we then obtained corresponding wind speed distributions Φ_u for the δt -averaged u values, and we used f_Q and Φ_u to calculate u_{th} by Eq. 4 (Fig. 2f). We chose the averaging interval $\delta t = 2$ s based on the typical response time of saltation to turbulent wind fluctuations [e.g., Anderson and Haff, 1988; McEwan and Willetts, 1991; Ma and Zheng, 2011], and we chose the analysis interval to represent the typical oscillation period for large-scale structures in an atmospheric boundary layer [e.g., Guala *et al.*, 2011].

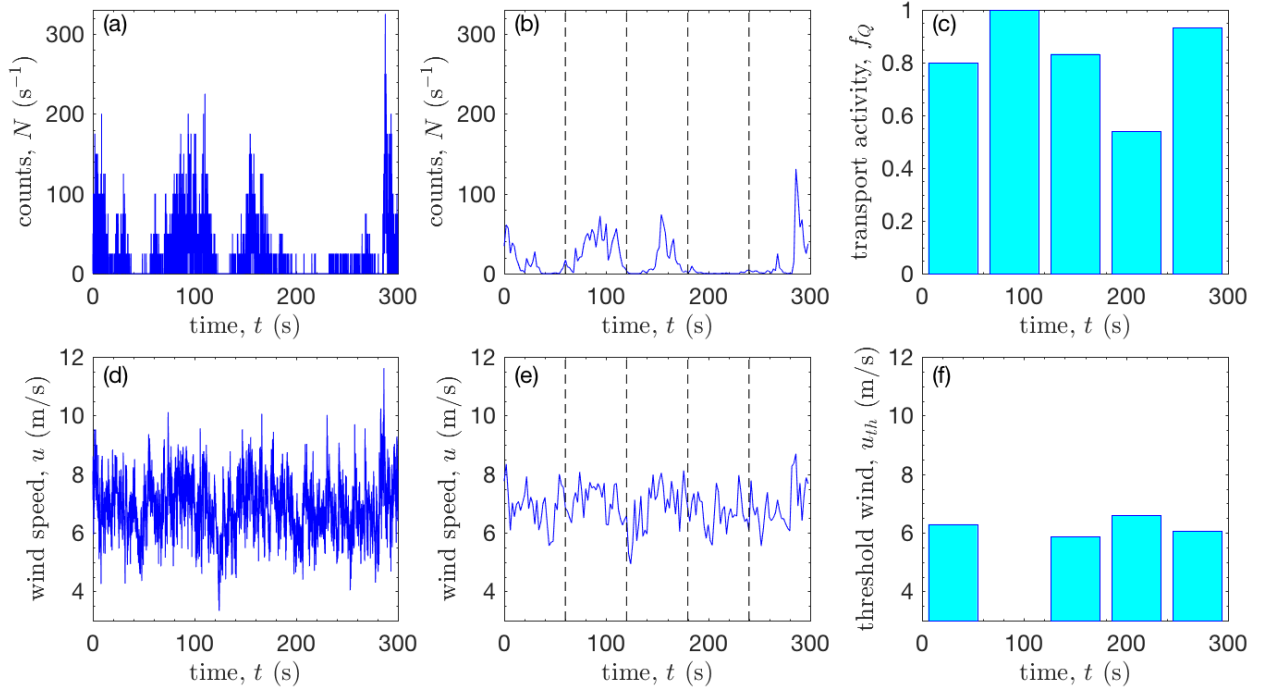


Figure 2. Sample measurements (Rancho Guadalupe, 24 March 2015, 13:31-13:36) to illustrate methods for calculating transport activity f_Q and effective threshold wind speed u_{th} . (a) Time series of total particle counts N . (b) $\delta t = 2$ s interval-averaged N time series. Dashed lines indicate $\Delta t = 1$ minute analysis intervals. (c) Transport activities f_Q , calculated as fraction of δt increments in each Δt for which $N > 0$, and corrected for false negatives. (d) Time series of streamwise wind speed u . (e) $\delta t = 2$ s interval-averaged u . Dashed lines again indicate Δt . (f) Resulting values of threshold wind speed u_{th} calculated by Eq. 4 from corresponding f_Q and wind speed distributions Φ_u for each Δt . u_{th} is undefined for $t = 60$ -120s when $f_Q = 1$.

We converted effective threshold wind speeds u_{th} to effective threshold shear velocities $u_{*,th}$ and stresses τ_{th} by the law-of-the-wall and the standard τ - u_* relationship:

$$u_{th} = \frac{u_{*,th}}{\kappa} \ln \left(\frac{z_u}{z_0} \right), \quad (6)$$

$$\tau_{th} = \rho_f u_{*,th}^2, \quad (7)$$

where z_0 is aerodynamic roughness height, $\kappa \approx 0.4$ is the von Karman parameter, ρ_f is air density, and u_{th} values were grouped into f_Q bins to facilitate uncertainty estimation (see Supporting Information Text S2). To justify use of the law-of-the-wall, which only applies to unidirectional and neutrally-stable conditions, our threshold calculations included only intervals with stability parameter $|z/L| \leq 0.2$, below which law-of-the-wall and Reynolds stress estimates of shear stress are roughly equivalent [Salesky *et al.*, 2012], and wind direction $|\theta| \leq 20^\circ$, where $\theta = 0^\circ$ is the mean sediment-transporting wind (see Martin and Kok [2017] for further explanation). Though effective z_0 [e.g., Sherman, 1992] and possibly κ [Li *et al.*, 2010] are known to change with saltation intensity, we assumed constant z_0 and κ in all calculations, based on a negligible observed change in z_0 with f_Q (see Supporting Information Text S3).

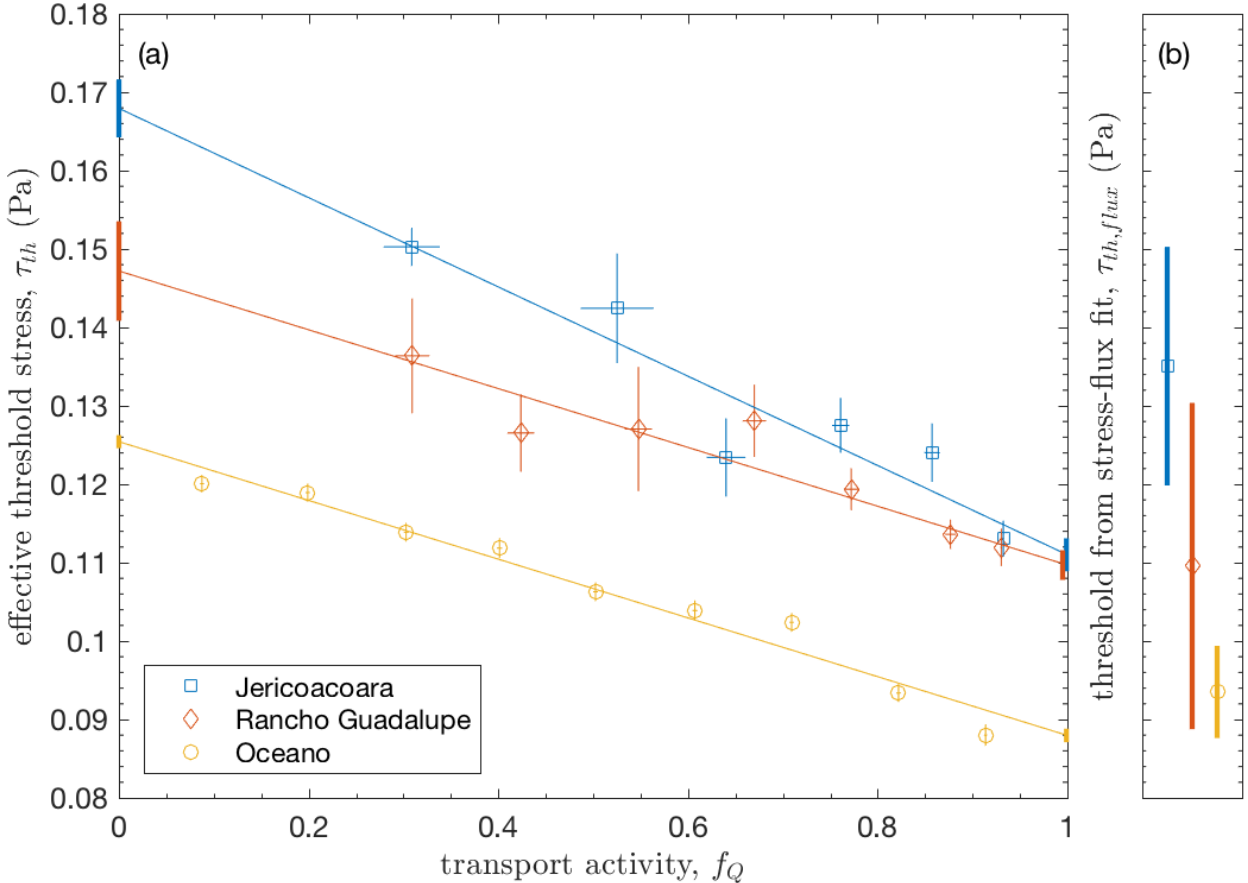


Figure 3. (a) Effective threshold stress τ_{th} versus transport activity f_Q . Error bars correspond to 1 standard error for binned values. Color-coded lines show least-squares fit to Eq. 5 at each field site. Vertical bars at $f_Q = 0$ provide estimates for fluid threshold τ_{ft} and its uncertainty from the linear fit; bars at $f_Q = 1$ are for impact threshold. (b) Thresholds $\tau_{th,flux}$ estimated by Eq. 8 from saltation flux measurements of *Martin and Kok* [2017]. Specific values for τ_{ft} , τ_{it} , and $\tau_{th,flux}$ are listed in Supporting Information Table S1.

4. Results

We use the methods described in Section 3 to calculate effective threshold stresses and saltation activities at our three field sites, which we then use to estimate fluid and impact threshold stresses and evaluate our hypotheses on dual threshold control of saltation activity described in Section 2.

As predicted by Eq. 5, we find that the effective threshold stress τ_{th} decreases linearly with saltation activity f_Q at each of the field sites (Fig. 3a). Based on Eq. 5, we calculate fluid and impact threshold stresses, τ_{ft} and τ_{it} , from the limiting effective threshold values for no transport ($f_Q \rightarrow 0$) and continuous transport ($f_Q \rightarrow 1$), as shown in Fig. 3a. These calculated τ_{ft} and τ_{it} are comparable to values from wind tunnel experiments for similar grain sizes [see Figs. 5 and 21 in *Kok et al.*, 2012]. Converting fluid and impact threshold stresses to threshold shear velocities by Eq. 6, we calculate threshold ratios $u_{*,it}/u_{*,ft} = 0.813 \pm 0.018$, 0.863 ± 0.027 , and

0.837 ± 0.007 at Jericoacoara, Rancho Guadalupe, and Oceano, respectively, which are consistent with laboratory measurements [Bagnold, 1937] and numerical predictions [Kok, 2010a] of $u_{*,it}/u_{*,ft} \approx 0.82$ (i.e., $\tau_{it}/\tau_{ft} \approx 0.67$) (See Supporting Information Text S4).

To further test our theory describing the relative influence of fluid and impact thresholds on saltation activity, we compare measured saltation activities f_Q to those expected for fluid ($f_{Q,ft}$), impact ($f_{Q,it}$), and dual ($f_{Q,dual}$) threshold control of saltation occurrence. We predict these expected transport activities by applying Eqs. 1-3 to measured wind time series $u(t)$, relative to fluid and impact threshold wind speeds calculated from τ_{ft} and τ_{it} by Eqs. 6 and 7 (Fig. 1). As expected, dual threshold control provides the best explanation for the observed transport activity at all sites, while fluid and impact threshold control respectively under- and over-predict transport activity (Fig. 4). Also, $f_{Q,dual}$ approaches $f_{Q,ft}$ near the limit of no transport where fluid threshold is expected to dominate ($f_Q \rightarrow 0$ in Eq. 5); conversely, $f_{Q,dual}$ approaches $f_{Q,it}$ in the limit of continuous transport where impact threshold is expected to dominate ($f_Q \rightarrow 1$ in Eq. 5). Though $f_{Q,dual}$ does diverge from observations for small and large f_Q , chi-square tests indicate that the dual-threshold hypothesis provides by far the best predictions for saltation activity (see Supporting Information Text S5).

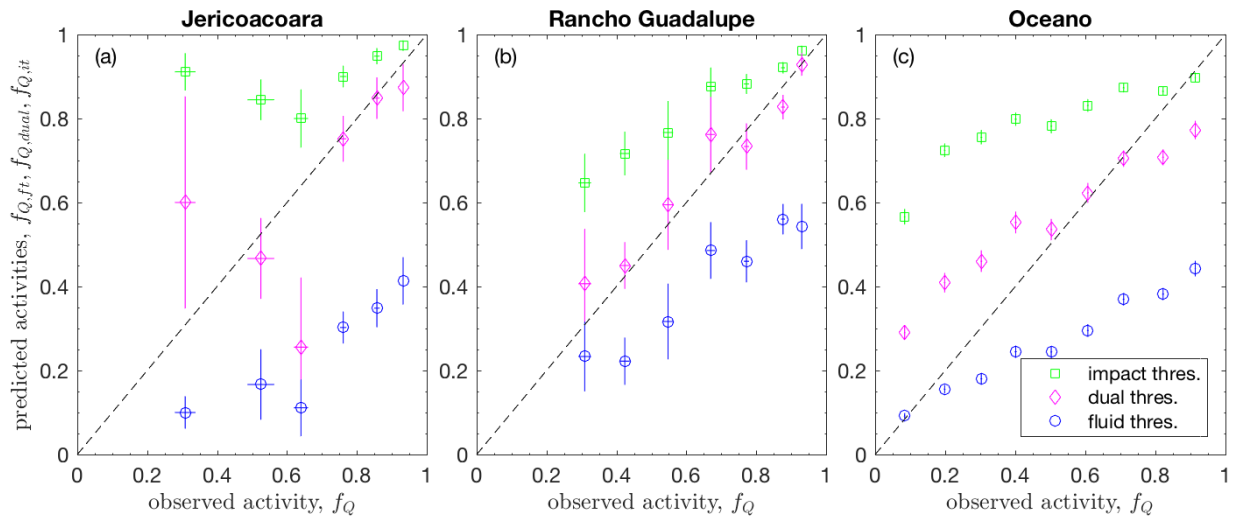


Figure 4. Predicted transport activities for impact threshold control $f_{Q,it}$ (Eq. 2), dual threshold control $f_{Q,dual}$ (Eq. 3), and fluid threshold control $f_{Q,ft}$ (Eq. 1), versus observed transport activities f_Q .

5. Discussion

Our results provide the first field-based evidence for the occurrence of separate fluid and impact thresholds in aeolian saltation. Though fluid and impact thresholds for saltation initiation and cessation have long been theorized [e.g., Bagnold, 1937; Kok, 2010b] and measured in wind tunnel experiments [e.g., Iversen and Rasmussen, 1994], the difficulty of directly measuring threshold crossings in the field [e.g., Barchyn and Hugenholtz, 2011] has limited the ability of

past studies to resolve both thresholds. To overcome these limitations, we examined the combined statistical effect of fluid and impact thresholds on the frequency of saltation transport over one-minute time intervals, thereby avoiding the need to attribute individual threshold-crossing events. In particular, we considered how dual thresholds together control the occurrence of saltation transport (Eqs. 1-3), such that the statistically-defined effective threshold [Stout and Zobeck, 1997; Stout, 2004] combines contributions of fluid and impact thresholds weighted by the observed saltation activity (Eq. 5). By fitting observed saltation activities and effective thresholds to Eq. 5, we calculated distinct fluid and impact threshold stresses at three field sites (Fig. 3). Then, we showed how wind fluctuations around these dual thresholds mostly explain observed saltation activities, except in limiting cases of infrequent ($f_Q \rightarrow 0$) or near-continuous ($f_Q \rightarrow 1$) transport, for which the respective fluid or impact thresholds alone provide sufficient predictive power (Fig. 4).

Our analysis strongly supports the existence of separate fluid and impact thresholds that together control saltation activity, but these findings could depend on the selection of averaging intervals δt for our calculations (Fig. 2) [Stout, 1998; Wiggs *et al.*, 2004; Barchyn and Hugenholtz, 2011]. Saltation is more likely to occur within longer δt increments (Fig. 2b), thus increasing f_Q (Fig. 2c). Longer δt also decreases the amplitude of wind fluctuations (Fig. 2e), which reduces the range of measured effective thresholds u_{th} (Fig. 2f). To evaluate these effects for a range of δt (1-4 seconds) corresponding to typical saltation response times [e.g., Anderson and Haff, 1988; McEwan and Willetts, 1991; Ma and Zheng, 2011], we performed a sensitivity analysis (Supporting Information Text S6). Though τ_{it} , τ_{ft} , and u_{*it}/u_{*ft} do vary with δt , these calculations remain broadly consistent with independent measurements [Bagnold, 1937; Kok, 2010b] regardless of δt . We also performed sensitivity analyses for analysis interval Δt , time of day (a proxy for atmospheric stability), and date (a proxy for grain size, which coarsened through time at Oceano), but found no systematic trends (Supporting Information Text S6 and S7). Nonetheless, further work is needed to understand the sensitivity of thresholds to atmospheric stability [e.g., Frank and Kocurek, 1994], soil texture [e.g., Greeley and Iversen, 1985], soil moisture [e.g., Davidson-Arnott *et al.*, 2008] and other soil conditions [e.g., Webb *et al.*, 2016].

Recent wind tunnel measurements of bed surface shear stress τ_0 versus saltation flux Q [Walter *et al.*, 2014] support our interpretations of how fluid and impact thresholds govern saltation transport. Walter *et al.* found that, so long as saltation activity is continuous (i.e., $f_Q = 1$), τ_0 remains constant with changes in Q . By Owen's hypothesis [Owen, 1964], Walter *et al.* interpreted this constant τ_0 as implying a constant rate of wind momentum dissipation at the bed surface equal to the impact threshold stress τ_{it} . However, they also observed τ_0 to decrease monotonically from τ_{ft} to τ_{it} during the transition from no saltation to continuous saltation [Fig. 4 in Walter *et al.*, 2014]. This result implies that τ_0 , like effective threshold τ_{th} , is governed by changes in f_Q modulating the relative importance of fluid and impact thresholds, as in Eq. 5.

We can gain insight into the selection of threshold(s) for saltation flux modeling by comparing fluid and impact threshold stresses calculated here to independent "flux-based" threshold stresses $\tau_{th,flux}$ obtained by Martin and Kok [2017] from the zero-intercept of the linear fit to saltation flux Q versus shear stress τ , i.e.,

$$Q \propto (\tau - \tau_{th,flux}). \quad (8)$$

Notably, at all sites except Jericoacoara, values for $\tau_{th,flux}$ agree with our τ_{it} measurements within uncertainty ranges (Fig. 3), and in all cases $\tau_{th,flux}$ values are closer to τ_{it} than to τ_{ft} . Due to the relatively small difference between τ_{it} and τ_{ft} on Earth, wind speed distributions for time-averaged shear stresses greater than τ_{it} contain many instances of stress temporarily exceeding τ_{ft} and therefore initiating saltation [Kok, 2010a], so that fluid threshold will not significantly contribute to $\tau_{th,flux}$. Therefore, τ_{it} alone can serve as the *de facto* threshold for saltation in comparisons of saltation flux and shear stress measured over longer time intervals (i.e., 30 minutes), while τ_{ft} may merely serve as a rough boundary between intermittent and continuous saltation (Supporting Information Fig. S9). However, when the gap between fluid and impact thresholds is larger, as on Mars [Kok, 2010b] and several other planetary bodies [Pähzt and Durán, 2016], or for smaller particle sizes [Durán *et al.*, 2011], τ_{ft} may need to be included in saltation flux models.

These findings offer insight into how the threshold should be incorporated into models for sand and dust flux. Both fluid and impact threshold should be used together when considering high-frequency saltation fluctuations, for which the flux-based threshold appears to be strongly governed by averaging timescale [Martin *et al.*, 2013]. Dual thresholds should also be considered for modeling saltation on Mars [Kok, 2010b] or other planetary bodies [Pähzt and Durán, 2016] where the impact-fluid threshold ratio is much smaller than on Earth. However, when modeling saltation flux over longer analysis intervals (i.e., 30 minutes), such as in large-scale models for wind erosion [e.g., Chepil, 1945], dune migration [e.g., Fryberger *et al.*, 1979], and dust emission [e.g., Gillette and Passi, 1988], our results indicate that use of the impact threshold alone is sufficient. Because most aeolian saltation likely occurs during near-threshold conditions [Jerolmack and Brzinski, 2010], for which predicted saltation flux depends strongly on the selected threshold (i.e., by Eq. 8), adoption of the impact threshold, instead of the commonly-used higher fluid threshold [e.g., Iversen and White, 1982; Marticorena and Bergametti, 1995; Shao, 2008], could substantially increase some predictions for saltation flux and associated dust emission.

6. Conclusion

Here we offered the first field-based evidence of distinct fluid and impact thresholds for the respective initiation and cessation of aeolian saltation. The measured ratio of these thresholds is consistent with past laboratory and numerical studies of dual thresholds. The presence of two distinct thresholds causes high-frequency (~ 1 min) fluctuations in transport activity to be controlled by both the fluid and impact thresholds. When saltation is active a small fraction of the time, fluid threshold dominates. As saltation activity increases, so too does the relative contribution of impact threshold, until it dominates under near-continuous transport conditions. However, our results indicate that the impact threshold alone is sufficient for explaining the time-averaged (~ 30 mins) momentum dissipation during terrestrial saltation and therefore the zero-intercept of saltation flux laws. Consequently, parameterizations of sand and dust transport in models, which currently predominantly use the fluid threshold, should instead use the impact threshold.

ACKNOWLEDGEMENTS. U.S. National Science Foundation (NSF) Postdoctoral Fellowship EAR-1249918 to R.L.M., NSF grant AGS-1358621 to J.F.K., and ARO grant W911NF-15-1-0417 to J.F.K. supported this research. Oceano Dunes State Vehicular Recreation Area, Rancho Guadalupe Dunes Preserve, and Jericoacoara National Park provided essential site access and support. We thank Marcelo Chamecki for advice on treatment of wind data, Chris Hugenoltz and Tom Barchyn for equipment help, Doug Jerolmack for lab access for grain-size analysis, and Jean Ellis, Paulo Sousa, Peter Li, Francis Turney, Arkayan Samaddar, and Livia Freire for field assistance. Jericoacoara fieldwork is registered with the Brazilian Ministry of the Environment (#46254-1 to J. Ellis). Data included in the analysis for this paper is described in Supporting Information Dataset S1 and can be found on the Zenodo data repository at <http://doi.org/10.5281/zenodo.321417>.

References

Anderson, R. S., and P. K. Haff (1988), Simulation of eolian saltation, *Science*, 241(4867), 820–823, doi:10.1126/science.241.4867.820.

Ayoub, F., J.-P. Avouac, C. E. Newman, M. I. Richardson, A. Lucas, S. Leprince, and N. T. Bridges (2014), Threshold for sand mobility on Mars calibrated from seasonal variations of sand flux, *Nat. Commun.*, 5, 5096.

Baas, A. C. W. (2008), Challenges in aeolian geomorphology: Investigating aeolian streamers, *Geomorphology*, 93(1–2), 3–16, doi:10.1016/j.geomorph.2006.12.015.

Bagnold, R. A. (1937), The transport of sand by wind, *Geogr. J.*, 89(5), 409–438, doi:10.2307/1786411.

Bagnold, R. A. (1941), *The Physics of Blown Sand and Desert Dunes*, Dover, London.

Barchyn, T. E., and C. H. Hugenholtz (2011), Comparison of four methods to calculate aeolian sediment transport threshold from field data: Implications for transport prediction and discussion of method evolution, *Geomorphology*, 129(3–4), 190–203, doi:10.1016/j.geomorph.2011.01.022.

Barchyn, T. E., C. H. Hugenholtz, B. Li, C. McKenna Neuman, and R. S. Sanderson (2014a), From particle counts to flux: Wind tunnel testing and calibration of the “Wenglor” aeolian sediment transport sensor, *Aeolian Res.*, 15, 311–318, doi:10.1016/j.aeolia.2014.06.009.

Barchyn, T. E., R. L. Martin, J. F. Kok, and C. H. Hugenholtz (2014b), Fundamental mismatches between measurements and models in aeolian sediment transport prediction: The role of small-scale variability, *Aeolian Res.*, 15, 245–251, doi:10.1016/j.aeolia.2014.07.002.

Bevington, P. R., and D. K. Robinson (2003), *Data reduction and error analysis for the physical sciences*, 3rd ed., McGraw-Hill, New York.

van Boxel, J. H., G. Sterk, and S. M. Arens (2004), Sonic anemometers in aeolian sediment transport research, *Geomorphology*, 59(1–4), 131–147, doi:10.1016/j.geomorph.2003.09.011.

Bridges, N. T., F. Ayoub, J.-P. Avouac, S. Leprince, A. Lucas, and S. Mattson (2012), Earth-like sand fluxes on Mars, *Nature*, 485(7398), 339–342, doi:10.1038/nature11022.

Carneiro, M. V., K. R. Rasmussen, and H. J. Herrmann (2015), Bursts in discontinuous Aeolian saltation, *Sci. Rep.*, 5, doi:10.1038/srep11109.

Chepil, W. S. (1945), Dynamics of Wind Erosion. 2. Initiation of soil movement, *Soil Sci.*, 60(5), 397, doi:10.1097/00010694-194511000-00005.

Creyssels, M., P. Dupont, A. O. El Moctar, A. Valance, I. Cantat, J. T. Jenkins, J. M. Pasini, and K. R. Rasmussen (2009), Saltating particles in a turbulent boundary layer: Experiment and theory, *J. Fluid Mech.*, 625, 47–74, doi:10.1017/S0022112008005491.

Davidson-Arnott, R. G. D., and B. O. Bauer (2009), Aeolian sediment transport on a beach: Thresholds, intermittency, and high frequency variability, *Geomorphology*, 105(1–2), 117–126, doi:10.1016/j.geomorph.2008.02.018.

Davidson-Arnott, R. G. D., K. MacQuarrie, and T. Aagaard (2005), The effect of wind gusts, moisture content and fetch length on sand transport on a beach, *Geomorphology*, 68(1–2), 115–129, doi:10.1016/j.geomorph.2004.04.008.

Davidson-Arnott, R. G. D., Y. Yang, J. Ollerhead, P. A. Hesp, and I. J. Walker (2008), The effects of surface moisture on aeolian sediment transport threshold and mass flux on a beach, *Earth Surf. Process. Landf.*, 33(1), 55–74, doi:10.1002/esp.1527.

Durán, O., P. Claudin, and B. Andreotti (2011), On aeolian transport: Grain-scale interactions, dynamical mechanisms and scaling laws, *Aeolian Res.*, 3(3), 243–270, doi:10.1016/j.aeolia.2011.07.006.

Frank, A., and G. Kocurek (1994), Effects of atmospheric conditions on wind profiles and aeolian sand transport with an example from White Sands National Monument, *Earth Surf. Process. Landf.*, 19(8), 735–745, doi:10.1002/esp.3290190806.

Fryberger, S. G., G. Dean, and E. D. McKee (1979), Dune forms and wind regime, in *A Study of Global Sand Seas, U.S. Geological Survey Professional Paper 1052*, edited by E. D. McKee, pp. 137–170, USGS, Washington, D. C.

Gillette, D. A., and R. Passi (1988), Modeling dust emission caused by wind erosion, *J. Geophys. Res. Atmospheres*, 93(D11), 14233–14242, doi:10.1029/JD093iD11p14233.

Greeley, R., and J. D. Iversen (1985), *Wind as a Geological Process on Earth, Mars, Venus and Titan*, Cambridge University Press, New York.

Guala, M., M. Metzger, and B. J. McKeon (2011), Interactions within the turbulent boundary layer at high Reynolds number, *J. Fluid Mech.*, 666, 573–604, doi:10.1017/S0022112010004544.

Iversen, J. D., and K. R. Rasmussen (1994), The effect of surface slope on saltation threshold, *Sedimentology*, 41(4), 721–728, doi:10.1111/j.1365-3091.1994.tb01419.x.

Iversen, J. D., and B. R. White (1982), Saltation threshold on Earth, Mars and Venus, *Sedimentology*, 29(1), 111–119, doi:10.1111/j.1365-3091.1982.tb01713.x.

Jerolmack, D. J., and T. A. Brzinski (2010), Equivalence of abrupt grain-size transitions in alluvial rivers and eolian sand seas: A hypothesis, *Geology*, 38(8), 719–722, doi:10.1130/G30922.1.

Kok, J. F. (2010a), An improved parameterization of wind-blown sand flux on Mars that includes the effect of hysteresis, *Geophys. Res. Lett.*, 37(12), L12202, doi:10.1029/2010GL043646.

Kok, J. F. (2010b), Difference in the wind speeds required for initiation versus continuation of sand transport on Mars: Implications for dunes and dust storms, *Phys. Rev. Lett.*, 104(7), 74502, doi:10.1103/PhysRevLett.104.074502.

Kok, J. F., E. J. R. Parteli, T. I. Michaels, and D. B. Karam (2012), The physics of wind-blown sand and dust, *Rep. Prog. Phys.*, 75, 106901, doi:10.1088/0034-4885/75/10/106901.

Kok, J. F., N. M. Mahowald, G. Fratini, J. A. Gillies, M. Ishizuka, J. F. Leys, M. Mikami, M.-S. Park, S.-U. Park, R. S. Van Pelt, and T. M. Zobeck (2014), An improved dust emission model – Part 1: Model description and comparison against measurements, *Atmos Chem Phys*, 14(23), 13023–13041, doi:10.5194/acp-14-13023-2014.

Li, B., D. J. Sherman, E. J. Farrell, and J. T. Ellis (2010), Variability of the apparent von Karman parameter during aeolian saltation, *Geophys. Res. Lett.*, 37(15), L15404, doi:10.1029/2010GL044068.

Li, Z., X. Zhao, and W. Huang (2008), A stochastic model for initial movement of sand grains by wind, *Earth Surf. Process. Landf.*, 33(11), 1796–1803, doi:10.1002/esp.1638.

Lindhorst, S., and C. Betzler (2016), The climate-archive dune: Sedimentary record of annual wind intensity, *Geology*, 44(9), 711–714, doi:10.1130/G38093.1.

Lorenz, R. D., and J. R. Zimbelman (2014), *Dune Worlds*, Springer, Heidelberg.

Ma, G. S., and X. J. Zheng (2011), The fluctuation property of blown sand particles and the wind-sand flow evolution studied by numerical method, *Eur. Phys. J. E*, 34(5), doi:10.1140/epje/i2011-11054-3.

Marticorena, B., and G. Bergametti (1995), Modeling the atmospheric dust cycle: 1. Design of a soil-derived dust emission scheme, *J. Geophys. Res. Atmospheres*, 100(D8), 16415–16430, doi:10.1029/95JD00690.

Martin, R. L., and J. F. Kok (2017), Wind-invariant saltation heights imply linear scaling of aeolian saltation flux with shear stress, *Sci. Adv.*, in review.

Martin, R. L., T. E. Barchyn, C. H. Hugenholtz, and D. J. Jerolmack (2013), Timescale dependence of aeolian sand flux observations under atmospheric turbulence, *J. Geophys. Res. Atmospheres*, 118(16), 9078–9092, doi:10.1002/jgrd.50687.

Martin, R. L., J. F. Kok, and M. Chamecki (2017), Comprehensive field campaigns illustrate new methods for characterizing high-frequency variability in aeolian saltation flux, *arXiv:1609.08707v2*.

McEwan, I. K., and B. B. Willetts (1991), Numerical model of the saltation cloud., *Acta Mech. Suppl.*, 1, 53–66.

Nickling, W. G. (1988), The initiation of particle movement by wind, *Sedimentology*, 35(3), 499–511, doi:10.1111/j.1365-3091.1988.tb01000.x.

Owen, P. R. (1964), Saltation of uniform grains in air, *J. Fluid Mech.*, 20(2), 225–242, doi:10.1017/S0022112064001173.

Pähzt, T., and O. Durán (2016), Fluid forces or impacts, what governs the entrainment of soil particles in sediment transport mediated by a Newtonian fluid?, *arXiv:1605.07306v4*.

Rice, M. A., I. K. McEwan, and C. E. Mullins (1999), A conceptual model of wind erosion of soil surfaces by saltating particles, *Earth Surf. Process. Landf.*, 24(5), 383–392, doi:10.1002/(SICI)1096-9837(199905)24:5<383::AID-ESP995>3.0.CO;2-K.

Salesky, S. T., M. Chamecki, and N. L. Dias (2012), Estimating the random error in eddy-covariance based fluxes and other turbulence statistics: the filtering method, *Bound.-Layer Meteorol.*, 144(1), 113–135, doi:10.1007/s10546-012-9710-0.

Schönfeldt, H. J. (2004), Establishing the threshold for intermittent aeolian sediment transport., *Meteorol. Z.*, 13(5), 437–444, doi:10.1127/0941-2948/2004/0013-0437.

Shao, Y. (2008), *Physics and Modelling of Wind Erosion*, Springer, The Netherlands.

Shao, Y., and H. Lu (2000), A simple expression for wind erosion threshold friction velocity, *J. Geophys. Res.*, 105(D17), 22437–22443, doi:200010.1029/2000JD900304.

Sherman, D. J. (1992), An equilibrium relationship for shear velocity and apparent roughness length in aeolian saltation, *Geomorphology*, 5(3–5), 419–431, doi:10.1016/0169-555X(92)90016-H.

Sherman, D. J., B. Li, J. T. Ellis, E. J. Farrell, L. P. Maia, and H. Granja (2013), Recalibrating aeolian sand transport models, *Earth Surf. Process. Landf.*, 38(2), 169–178, doi:10.1002/esp.3310.

Stout, J. E. (1998), Effect of averaging time on the apparent threshold for aeolian transport, *J. Arid Environ.*, 39(3), 395–401, doi:10.1006/jare.1997.0370.

Stout, J. E. (2004), A method for establishing the critical threshold for aeolian transport in the field, *Earth Surf. Process. Landf.*, 29(10), 1195–1207, doi:10.1002/esp.1079.

Stout, J. E., and T. M. Zobeck (1997), Intermittent saltation, *Sedimentology*, 44(5), 959–970, doi:10.1046/j.1365-3091.1997.d01-55.x.

Ungar, J. E., and P. K. Haff (1987), Steady state saltation in air, *Sedimentology*, 34(2), 289–299, doi:10.1111/j.1365-3091.1987.tb00778.x.

Walter, B., S. Horender, C. Voegeli, and M. Lehning (2014), Experimental assessment of Owen's second hypothesis on surface shear stress induced by a fluid during sediment saltation, *Geophys. Res. Lett.*, 41(17), 6298–6305, doi:10.1002/2014GL061069.

Webb, N. P., M. S. Galloza, T. M. Zobeck, and J. E. Herrick (2016), Threshold wind velocity dynamics as a driver of aeolian sediment mass flux, *Aeolian Res.*, 20, 45–58.

Wiggs, G. F. S., R. J. Atherton, and A. J. Baird (2004), Thresholds of aeolian sand transport: establishing suitable values, *Sedimentology*, 51(1), 95–108, doi:10.1046/j.1365-3091.2003.00613.x.

Supporting Information for

Field measurements demonstrate distinct initiation and cessation thresholds governing aeolian sediment transport flux

Raleigh L. Martin¹ and Jasper F. Kok¹

¹Department of Atmospheric and Oceanic Sciences, University of California, Los Angeles, CA 90095

Contents of this file

Text S1 to S8

Figures S1 to S9

Tables S1 to S5

Additional Supporting Information (Files uploaded separately)

Caption for Datasets S1

Introduction

In this supporting document, we describe details associated with the analyses presented in the main paper. Text S1 describes a correction to account for false negatives when calculating saltation activity, Text S2 explains methods for calculating and propagating uncertainty in threshold estimates, Text S3 presents calculations for the roughness height used to convert wind speed to shear stress, Text S4 details methods for computing fluid and impact thresholds, Text S5 compares statistical tests for viability of different threshold models, Text S6 justifies our choices of averaging and analysis intervals, Text S7 considers the possibility of diurnal or secular trends affecting threshold variability, and Text S8 lists variables used in the main paper and Supporting Information Text. Supporting Figures (S1-S9) and Tables (S1-S5) accompany this text. In addition, we describe Supporting Dataset S1, which contains the threshold and saltation activity values calculated for this analysis.

Text S1. Accounting for false negatives in calculation of saltation activity

Here, we derive a method to account for the possibility of “false negatives” (i.e., instances in which saltation transport occurs but is not detected) when computing saltation activity f_Q . To do so, we distinguish the measured saltation detection rate f_D from the actual saltation activity f_Q . We compute f_D as the fraction of averaging intervals δt in each analysis interval Δt for which total particle counts rate N is nonzero. We then estimate f_Q from f_D by calculating the expected rate of false negatives for particle arrivals occurring as a Poisson counting process. We detail this procedure below.

By Bayes Theorem, we have:

$$f_{D|Q} = \frac{f_D f_{Q|D}}{f_Q}, \quad (\text{S1})$$

where $f_{D|Q}$ is the conditional probability of detecting transport when it is active, and $f_{Q|D}$ is the probability that transport is actually active when it has been detected. We observed that the Wenglor optical particle counters did not produce “false positives,” i.e. that detection necessarily implied transport and therefore that $f_{Q|D} = 1$. However, we found that during conditions of weak transport or few Wenglor counters, false negatives could occur with some regularity due to the limited sampling volume of individual counters. Denoting these false negatives as $f_{\sim D|Q}$ and noting that $f_{\sim D|Q} + f_{D|Q} = 1$, we can restate Eq. S1 as:

$$f_Q = \frac{f_D}{1 - f_{\sim D|Q}}. \quad (\text{S2})$$

To estimate the rate of false negatives $f_{\sim D|Q}$, we treat particle arrivals as a Poisson counting process. For such a process:

$$f_{\sim D|Q} = \exp(-\lambda), \quad (\text{S3})$$

where λ is the average arrival rate of particles per δt averaging interval at times when transport is active. We calculate λ as:

$$\lambda = \bar{N} \delta t / f_D, \quad (\text{S4})$$

where \bar{N} is the mean particle counts rate during the analysis interval $\Delta t = 1$ minute. Combining Eqs. S2-S4, we have:

$$f_Q = \frac{f_D}{1 - \exp(-\lambda)} = \frac{f_D}{1 - \exp(-\bar{N} \delta t / f_D)}. \quad (\text{S5})$$

The effect of the false negative correction in computing f_Q can be seen in Fig. S1. During strong transport, λ is large so $f_Q \approx f_D$ in Eq. S5. However, when transport is weak, δt is small, or the number of Wenglors are few, λ can be much smaller than 1, and therefore the correction causes f_Q to significantly exceed f_D .

Text S2. Estimation of uncertainties for effective threshold wind speeds, shear velocities, and shear stresses

To facilitate uncertainty estimation for computed effective thresholds, we combined effective threshold wind speed values u_{th} from individual Δt analysis intervals into bins defined by ranges of flux activity f_Q . For each bin, we computed bin-averaged threshold and activity values for u_{th} and f_Q , then we calculated their uncertainties from the standard errors of values in each bin.

When converting each bin-averaged effective threshold wind speed u_{th} to an effective threshold shear velocity $u_{*,th}$ and shear stress τ_{th} , we performed error propagation to estimate uncertainties in $u_{*,th}$ and τ_{th} .

S2.1. Creation of flux activity bins

For each site, we grouped values of u_{th} for individual Δt together into bins covering ranges of f_Q . To accommodate the uneven spread of data points across the range of possible f_Q , we allowed for creation of bins covering varying ranges of f_Q . These criteria were established to balance the need for a sufficient number of data points in each bin with the need to limit the maximum width of the bins. The procedure for generating the binned values for each site is as follows:

- (1) Sort all u_{th} data points in order of increasing f_Q . Because the effective threshold calculation (Eq. 1) assumes intermittent transport conditions, exclude data points with $f_Q < 0.05$ and $f_Q > 0.95$.
- (2) Starting from the lowest remaining f_Q , add data points to the bin, until the following criteria are achieved for the bin
 - a. $\max(f_Q) - \min(f_Q) \geq 0.1$ (minimum bin width), AND
 - b. There are at least 3 points in the bin OR $\max(f_Q) - \min(f_Q) > 0.2$ (maximum bin width).
- (3) Once the bin is full, repeat step 2 for the next bin.

S2.2. Determination of mean values and uncertainties for each flux activity bin

For each bin i , we determined the mean value for flux activity $f_{Q,i}$ and its uncertainty $\sigma_{f_{Q,i}}$ as:

$$f_{Q,i} = \sum_j f_{Q,j} / N_i, \quad (S6)$$

$$\sigma_{f_{Q,i}} = \frac{\sqrt{\sum_j (f_{Q,j} - f_{Q,i})^2}}{\sqrt{N_i}}, \quad (S7)$$

where $f_{Q,j}$ are the individual values of flux activity in the bin and N_i is the total number of values in the bin. Eq. S7 was computed based on the typical formulation for the standard error [Eq. 4.14 in *Bevington and Robinson, 2003*]. Similarly, the mean effective threshold wind speed $u_{th,i}$ and its uncertainty $\sigma_{u_{th,i}}$ are:

$$u_{th,i} = \sum_j u_{th,j} / N_i, \quad (S8)$$

$$\sigma_{u_{th,i}} = \frac{\sqrt{\sum_j (u_{th,j} - u_{th,i})^2}}{\sqrt{N_i}}, \quad (S9)$$

where $u_{th,j}$ are the individual values of effective threshold in the bin.

S2.3. Estimation of uncertainties for effective threshold shear velocity and shear stress

We converted binned values for effective threshold wind speed $u_{th,i}$ to effective threshold shear velocity $u_{*,th}$ by Eq. 6 and to effective threshold stress τ_{th} by Eq. 7. In Eq. 6, we calculated aerodynamic roughness heights z_0 in Eq. 6 for each site based on wind velocity profiles for zero transport, and we assumed the standard von Karman parameter $\kappa \approx 0.4$. In Supporting Information Text S3 below, we justify the use of constant values z_0 and κ , despite the known tendencies of these values to change systematically with saltation flux. In Eq. 7, we set the air density ρ_f based on the mean temperature at each site [Martin and Kok, 2017].

Using the error propagation formula [Eq. 3.14 in Bevington and Robinson, 2003], we propagated effective threshold wind speed uncertainty $\sigma_{u_{th}}$ and roughness length uncertainty σ_{z_0} (calculated in Supporting Information Text S3 below) to derive uncertainty in threshold shear velocity $\sigma_{u_{*,th}}$ and threshold stress $\sigma_{\tau_{th}}$:

$$\sigma_{u_{*,th}} = \frac{u_{*,th}}{u_{th}} \sqrt{\sigma_{u_{th}}^2 + \frac{\ln^2(\sigma_{z_0})}{\ln^2(z_u/z_0)} u_{*,th}^2}, \quad (S10)$$

$$\sigma_{\tau_{th}} = 2\rho_f u_{*,th} \sigma_{u_{*,th}}. \quad (S11)$$

Text S3. Determination of aerodynamic roughness height and its sensitivity to variation in saltation activity

Here, we describe methods for determining aerodynamic roughness height z_0 . Then we evaluate the possibility of systematic variation in saltation-influenced effective roughness height z_s with transport activity f_Q . To evaluate sensitivity of saltation-influenced von Karman parameter κ_s to f_Q , we assume that such von Karman sensitivity will be reflected in the sensitivity of z_s .

S3.1. Estimation of aerodynamic roughness height z_0

Under neutrally stable conditions with negligible saltation, the aerodynamic roughness height z_0 describes the zero-intercept height of a linear fit to the vertical profile of horizontal wind versus the logarithm of wind height. In practice, we found that wind profile fits to calculate z_0 showed very large variability due to large deviations from expected logarithmic law-of-the-wall profiles resulting from convective instability during periods of non-saltation (see Fig. S2 in *Martin and Kok* [2017]).

To avoid the problem of unstable profiles, we instead considered the trend in effective roughness height z_s , which is influenced both by aerodynamic conditions and by saltation-induced roughness [Sherman, 1992], versus total saltation flux Q . (Methods for estimating Q are described in *Martin and Kok* [2017] and *Martin et al.* [2017].) For successive 30-minute intervals, we estimated z_s by manipulating the law-of-the-wall:

$$z_s = z_U \exp\left(-\frac{\kappa \bar{u}}{u_{*,Re}}\right), \quad (\text{S12})$$

where \bar{u} is the mean wind speed for anemometer height z_U during the 30-minute interval, $\kappa = 0.4$ is the von Karman parameter, and $u_{*,Re}$ is the shear velocity determined from the Reynolds stress method [*Martin and Kok*, 2017]. We calculated z_s by Eq. S12 over 30-minute intervals, instead of the $\Delta t = 1$ minute analysis intervals applied elsewhere in this paper, because $u_{*,Re}$ is ill-defined for $\Delta t = 1$ minute [*van Boxel et al.*, 2004].

Fig. S2 shows the variation in z_s with Q for each site. The logarithm of z_s increases linearly with Q up to $Q \approx 30 \text{ gm}^{-1}\text{s}^{-1}$. Performing a linear fit to $\ln(z_s)$ versus Q over this range, we estimate z_0 as the zero-intercept value of this fit, yielding values of $0.707 \times 10^{-4} \text{ m}$, $1.420 \times 10^{-4} \text{ m}$, and $0.993 \times 10^{-4} \text{ m}$, for Jericoacoara, Rancho Guadalupe, and Oceano, respectively. Associated uncertainties in log-space, i.e. $\sigma_{\ln(z_0)}$, are 0.115, 0.137, and 0.128, for Jericoacoara, Rancho Guadalupe, and Oceano, respectively.

S3.2. Sensitivity of effective roughness height z_s to changes in saltation activity f_Q

Values of z_0 as determined above were used for conversion of threshold wind speed u_{th} to threshold shear velocity $u_{*,th}$ and shear stress τ_{th} as described in Eqs. 6 and 7. However, such use of z_0 for this conversion may have failed to account for increase in the effective roughness length z_s with saltation intensity, thereby leading to underestimation of $u_{*,th}$ as compared to actual values.

To evaluate whether variation in z_s could have influenced our results, we directly compared measured values of z_s to f_Q over 30-minute intervals. Such comparison was only possible at Oceano, where 30-minute values of f_Q covered the full range of activities from 0 to 1. The result

of this comparison is shown in Fig. S3. Notably, there appears to be a negligible variation in z_s with f_Q . We confirm this lack of trend by performing a linear fit to $\ln(z_s)$ versus f_Q . The best fit for this slope, -0.339 ± 0.174 , indicates a weak negative trend. Though such a result seems at odds with the obvious increase in z_s with Q (Fig. S2), we note that most intermittent transport, i.e., $0.05 < f_Q < 0.95$, corresponds to relatively small saltation fluxes, for which the deviation of z_s away from z_0 is negligible. We therefore assume that z_0 remains constant when converting from threshold wind speeds to threshold shear velocities and shear stresses.

S3.3. Sensitivity of effective von Karman parameter κ_s to changes in saltation activity f_Q

We did not directly evaluate sensitivity of κ_s to f_Q . Instead, we note that κ_s and z_s should display similar sensitivities to f_Q . Therefore, the lack of trend in z_s with f_Q suggests a lack of trend in κ_s with f_Q .

Text S4. Calculation of fluid and impact threshold stresses and shear velocities

To calculate fluid and impact threshold stresses, τ_{ft} and τ_{it} , at each field site, we performed linear fits to τ_{th} versus f_Q according to Eq. 5. Here, we detail the fitting procedure to obtain τ_{ft} , τ_{it} , and the uncertainty for these values. Then, we describe the calculation of the threshold shear velocity ratio and its uncertainty.

S4.1. Calculation of fluid and impact thresholds by linear fit to saltation activity versus effective threshold stress

Following Eqs. 6.12, 6.21, 6.22, and 7.23 in *Bevington and Robinson* [2003], we performed a linear fit to τ_{th} versus f_Q , i.e.,

$$\tau_{th} = a + b f_Q, \quad (\text{S13})$$

where a is the fitting intercept and b is the fitting slope; σ_a , σ_b , and σ_{ab}^2 are their respective uncertainties and covariance.

Based on the linear fit (Eq. S13), fluid and impact thresholds were calculated for each site from the best fit values corresponding respectively to $f_Q = 0$ and $f_Q = 1$, i.e.:

$$\tau_{ft} = a, \quad (\text{S14})$$

$$\tau_{it} = a + b. \quad (\text{S15})$$

Corresponding uncertainties in these values were then computed as:

$$\sigma_{\tau_{ft}} = \sigma_a, \quad (\text{S16})$$

$$\sigma_{\tau_{it}} = \sqrt{\sigma_a^2 + \sigma_b^2 + 2\sigma_{ab}^2}. \quad (\text{S17})$$

S4.2. Calculation of impact/fluid threshold shear velocity ratio and its uncertainty

The ratio of impact and fluid threshold shear velocities and the uncertainty of this ratio were calculated from τ_{ft} , τ_{it} , $\sigma_{\tau_{ft}}$, and $\sigma_{\tau_{it}}$ by error propagation [Eq. 3.14 in *Bevington and Robinson*, 2003] as:

$$\frac{u_{*it}}{u_{*ft}} = \sqrt{\frac{\tau_{it}}{\tau_{ft}}}, \quad (\text{S18})$$

$$\sigma_{u_{*it}/u_{*ft}} = \frac{1}{2} \sqrt{\frac{\sigma_{\tau_{it}}^2}{\tau_{it}\tau_{ft}} + \frac{\sigma_{\tau_{ft}}^2 \tau_{it}}{\sigma_{\tau_{ft}}^3}}. \quad (\text{S19})$$

Text S5. Chi-square tests for saltation activity control hypotheses

Here, we evaluate the quality of fluid $f_{Q,ft}$ (Eq. 1), impact $f_{Q,it}$ (Eq. 2), and dual $f_{Q,dual}$ (Eq. 3) threshold control predictions for saltation activity versus observations f_Q . To do so, we compute the reduced chi-square χ^2_v , which expresses the difference between predicted and measured values, normalized by the number of degrees of freedom v :

$$\chi^2_v = \frac{1}{v} \sum_i \frac{(f_{Q,i} - f_{Q,pred,i})^2}{\sigma_{f_{Q,pred,i}}^2}, \quad (\text{S20})$$

where the $f_{Q,i}$ refer to individual binned observations for saltation activity, the $f_{Q,pred,i}$ refer to the predictions by Eqs. 1-3, and the $\sigma_{f_{Q,pred,i}}$ are the standard errors for these predictions.

Because there are no fitting parameters for $f_{Q,pred,i}$ values, we set v simply as the number of $f_{Q,i}$ bins. The resulting χ^2_v values for fluid $f_{Q,ft}$, impact $f_{Q,it}$, and dual $f_{Q,dual}$ threshold control are respectively: 77.6, 49.2, and 1.4 at Jericoacoara; 27.8, 17.8, and 0.8 at Rancho Guadalupe; and 343.6, 422.6, and 41.6 at Oceano. These χ^2_v values indicate the favorability of the $f_{Q,dual}$ prediction at all sites.

Text S6. Selection and justification of averaging and analysis time intervals for calculations of saltation activity and effective threshold

Recognizing that calculations of saltation activity f_Q and effective threshold wind speed u_{th} are sensitive to averaging interval δt and analysis interval Δt [Stout, 1998; Barchyn and Hugenholz, 2011], here we provide physical explanations for our selection of these values, then we perform analyses to investigate the sensitivity of our results to the choice of these time scales and to justify these choices.

S6.1. Physical basis for selecting averaging and analysis intervals

Noting the possible sensitivity of u_{th} calculations to selection of δt and Δt , we chose these averaging and analysis timescales through consideration of saltation transport mechanics and the requirements of the statistical analysis. For averaging interval, we chose $\delta t = 2$ s to (1) match the typical 1-4 second response time of saltation to turbulent wind fluctuations [e.g., Anderson and Haff, 1988; McEwan and Willetts, 1991; Ma and Zheng, 2011], (2) optimize the agreement between observed transport activity f_Q and predicted transport activity for the dual-threshold hypothesis $f_{Q,dual}$ (Eq. 3), and (3) optimize the agreement between observed threshold ratio $u_{*,it}/u_{*,ft}$ and the expected value of $u_{*,it}/u_{*,ft} = 0.82$ [Bagnold, 1937; Kok, 2010a]. Fig. S4 shows a comparison of f_Q and $f_{Q,dual}$ for five choices of δt (1 s, 1.4 s, 2 s, 3 s, and 4 s) at Oceano, and Fig. S5 and Table S2 show the effect of these five δt on the ratio $u_{*,it}/u_{*,ft}$. The agreement between f_Q and $f_{Q,dual}$ increases with δt , but $u_{*,it}/u_{*,ft}$ begins to diverge from 0.82 for $\delta t > 2$ s. To balance these two effects, we therefore chose $\delta t = 2$ s for our analyses. Though this selection of δt is somewhat arbitrary, we show below in S6.2 that changing δt does not qualitatively affect the outcome of our analysis.

For the analysis interval Δt , we require a timescale that is much larger than seconds, because of the decoupling of spatially-separated wind and saltation time series over such short timescales [e.g., Baas, 2008]. Because the typical oscillation of large-scale structures in an atmospheric boundary layer is roughly 1 minute [e.g., Guala *et al.*, 2011], Φ_u and f_Q determined at or above this timescale should provide representative statistical snapshots of wind and saltation fluctuations. Therefore, we chose $\Delta t = 1$ minute to satisfy these statistical sampling requirements while maximizing the number of analysis windows.

S6.2. Sensitivity analysis for effect of averaging interval

To examine the effect of averaging interval δt on the relation between f_Q and u_{th} , we redo the analysis from Fig. 3a for five values of δt : 1 s, 1.4 s, 2 s, 3 s, and 4 s. The resulting plots for Oceano, where the data are most voluminous, are shown in Fig. S5. The computed limiting values of fluid threshold τ_{ft} , impact threshold τ_{it} , and threshold ratio $u_{*,it}/u_{*,ft}$, are provided in Table S2.

There are two effects of averaging interval δt . First, the probability of detecting particles in each averaging interval increases with δt . This “flux detection effect” increases f_Q with increasing δt , and therefore it decreases u_{th} by Eq. 4. Second, by averaging over extreme events, the distribution of wind speeds Φ_u narrows with increasing δt . For small f_Q , this “wind distribution effect” will decrease u_{th} with increasing δt ; for large f_Q , it will increase u_{th} with increasing δt .

The outcome of these two effects can be seen in Fig. S5. The fluid threshold τ_{ft} , which corresponds to the lower limit $f_Q \rightarrow 0$, displays a substantial decrease in τ_{th} with increasing δt by a combination of the flux detection effect and the wind distribution effect. In contrast, the impact threshold τ_{it} , which corresponds to the upper limit $f_Q \rightarrow 1$, shows a minor increase in τ_{th} with increasing δt , as the increase from the wind distribution effect slightly outweighs the decrease by the flux detection effect. The combined result of decreasing τ_{ft} and increasing τ_{it} is to increase the threshold ratio $u_{*,it}/u_{*,ft}$ with increasing δt (Table S2).

S6.3. Sensitivity analysis for effect of analysis interval

Our choice of $\Delta t = 1$ minute was somewhat arbitrary: long enough to produce statistically-representative values for each analysis interval but short enough to generate a wide range of data points for analysis. In particular, making Δt much larger than 1 minute would have eliminated our ability to evaluate the full range of saltation activities at Jericoacoara and Rancho Guadalupe.

At Oceano, where the data are significantly more extensive, we are able to perform a sensitivity analysis to evaluate the effect of varying the analysis interval from 0.5 to 10 minutes. Holding averaging interval δt constant at 2 s, we consider 5 values for Δt at Oceano: 0.5 minutes, 1 minute, 2 minutes, 5 minutes, and 10 minutes. The resulting calculations of τ_{th} versus f_Q are shown in Fig. S6. The computed limiting values of fluid threshold τ_{ft} , impact threshold τ_{it} , and threshold ratio $u_{*,it}/u_{*,ft}$, are provided in Table S3. In all cases, the effect of changing Δt is negligible.

Text S7. Sensitivity of results to atmospheric and surface trends

In this section, we perform sensitivity analyses to indirectly consider the effects of variability of atmospheric and surface conditions on the determination of effective thresholds and limiting fluid and impact threshold values. To do this, we sort the data for Oceano in two ways: (1) by time of day, and (2) by date. Separating data by time of day is meant to capture diurnal variations in atmospheric and surface properties, such as atmospheric stability, humidity, and soil moisture. Separating data by date is meant to capture secular variations in grain size and sorting properties, as surface grain size tended to coarsen over time at Oceano.

S7.1. Sensitivity analysis by time of day

We separate the data into three components of the diurnal cycle that constituted most measured saltation flux at Oceano: 12-14h, 14-16h, and 16-18h. The resulting variation of effective threshold τ_{th} with transport activity f_Q is shown in Fig. S7, and corresponding limiting impact and fluid threshold values are given in Table S4. Though the three diurnal periods do show some variation in limiting fluid and impact threshold values, there is no systematic trend of increasing or decreasing thresholds through the course of the day. Furthermore, the separation between fluid and impact threshold is maintained throughout the day.

S7.2. Sensitivity analysis by date

We separate the data into three ranges of dates for which saltation flux was measured at Oceano: May 15-19, May 23-28, and June 1-4, 2015. The resulting variation of effective threshold τ_{th} with transport activity f_Q is shown in Fig. S8, and corresponding limiting impact and fluid threshold values are given in Table S5. Notably, there does appear to be an increase in τ_{it} for the May 23-28 and June 1-4 periods. This increase in the threshold corresponds to a slight coarsening of median grain diameter during these later periods (Table S5). This supports the notion that thresholds increase with grain diameter. In all cases, the trend of effective threshold τ_{th} decreasing with transport activity f_Q is maintained.

Text S8. List of variables

Below, we list all variables described in the manuscript. Typical units for variables are given in parentheses, if applicable.

S8.1. Variables in main text

τ = shear stress (Pa)
 τ_{ft} = fluid threshold shear stress (Pa)
 τ_{it} = impact threshold shear stress (Pa)
 u_{*it}/u_{*ft} = shear velocity threshold ratio
 τ_{th} = effective threshold stress (Pa)
 f_Q = saltation transport activity
 $u(t)$ = time series of horizontal wind speed (m/s)
 u_{ft} = fluid threshold wind speed (m/s)
 u_{it} = impact threshold wind speed (m/s)
 $f_{Q,ft}$ = expected saltation activity for transport dominated by fluid threshold
 $f_{Q,it}$ = expected saltation activity for transport dominated by impact threshold
 $f_{Q,dual}$ = expected saltation activity for transport mediated by both fluid and impact thresholds
 f_+ = fraction of time with $u \geq u_{ft}$
 f_{\sim} = fraction of time with $u_{it} \leq u < u_{ft}$
 f_{\downarrow} = fraction of time within $u_{it} \leq u < u_{ft}$ for which the most recent threshold crossing was a downward crossing of u_{ft}
 u_{th} = effective threshold wind speed (m/s)
 Φ_u = cumulative distribution of streamwise wind speed u
 N = vertically integrated saltation particle counts rate (counts/s)
 z_U = anemometer height above the sand surface (m)
 δt = averaging time interval (s)
 Δt = analysis time interval (minutes)
 $u_{*,th}$ = effective threshold shear velocity (m/s)
 κ = von Karman parameter
 z_0 = aerodynamic roughness height (m)
 z_s = effective roughness height, accounting for saltation-induced roughness (m)
 ρ_f = air density (kg/m³)
 z/L = stability parameter
 θ = angle of horizontal wind relative to dominant sand-transporting wind
 Q = saltation flux (g/m/s)
 τ_0 = bed surface shear stress (Pa)
 $\tau_{th,flux}$ = flux-based estimate of threshold stress (Pa)

S8.2. Additional variables in Supporting Information

f_D = saltation detection rate
 $f_{Q|D}$ = probability that transport is actually active when it has been detected
 $f_{D|Q}$ = conditional probability of detecting transport when it is active
 $f_{\sim D|Q}$ = conditional probability of not detecting transport when it is active
 λ = average arrival rate of particles (counts/s)

\bar{N} = mean vertically integrated saltation particle counts rate (counts/s)
 $f_{Q,i}$ = mean value for saltation transport activity for bin i
 $\sigma_{f_{Q,i}}$ = uncertainty in saltation transport activity for bin i
 $f_{Q,j}$ = individual values j of saltation activity in bin i
 N_i = number of values in bin i
 $u_{th,i}$ = mean value for effective threshold wind speed for bin i (m/s)
 $\sigma_{u_{th,i}}$ = uncertainty in effective threshold wind speed for bin i (m/s)
 $u_{th,j}$ = individual values j of effective threshold wind speed in bin i (m/s)
 $\sigma_{u_{*th}}$ = uncertainty in effective threshold shear velocity (m/s)
 $\sigma_{\tau_{th}}$ = uncertainty in effective threshold shear stress (Pa)
 \bar{u} = 30-minute mean wind speed (m/s)
 $\sigma_{\ln(z_0)}$ = natural log uncertainty in aerodynamic roughness height
 κ_s = effective von Karman parameter, accounting for saltation effects
 a = least squares linear fitting intercept
 σ_a = uncertainty in fitting intercept
 b = least squares linear fitting slope
 σ_b = uncertainty in fitting slope
 σ_{ab}^2 = covariance of fitting slope and intercept
 $\sigma_{\tau_{ft}}$ = uncertainty in fluid threshold stress (Pa)
 $\sigma_{\tau_{it}}$ = uncertainty in impact threshold stress (Pa)
 $\sigma_{u_{*it}/u_{*ft}}$ = uncertainty in shear velocity threshold ratio
 v = number of degrees of freedom for fitting
 χ^2_v = normalized chi-square value for goodness of fit
 $f_{Q,pred,i}$, predicted value of saltation activity for bin i
 d_{50} , median diameter of surface particles by volume (mm)

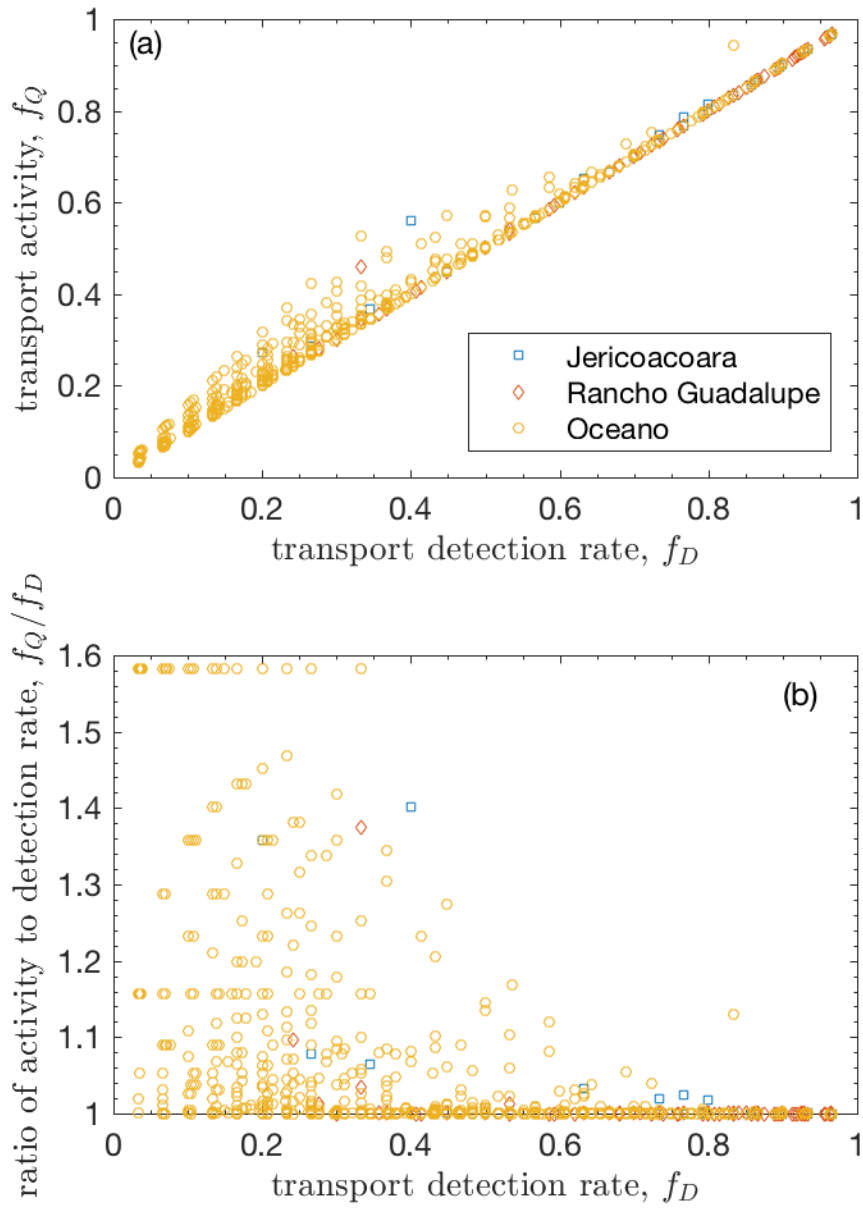


Figure S1. (a) Comparison of transport activity f_Q , which includes correction for estimated rate of false negatives (Eq. S5), to the actual transport detection rate f_D . (b) Ratio of transport activity to detection rate f_Q/f_D versus detection rate f_D , illustrating the relative magnitude of the correction for false negatives. This correction tends to be strongest when transport is weak, due to the higher probability of false negatives. The difference between f_Q and f_D is also affected by changes in the background particle detection rate, which can be affected by the number and height of Wenglor detectors and the nature of transport fluctuations.

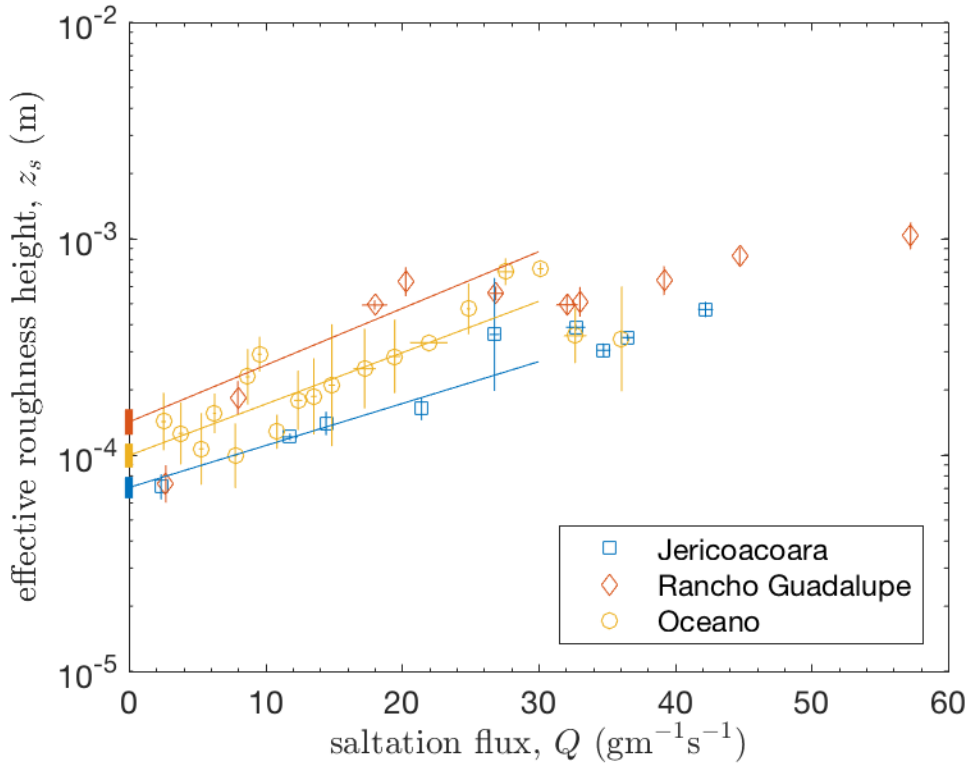


Figure S2. Comparison of effective roughness length z_s versus total saltation flux Q at each field site. We estimate z_0 as the zero-intercept of the linear fit of $\ln(z_s)$ versus Q at each site for $Q \leq 30 \text{ gm}^{-1}\text{s}^{-1}$, indicated by the thin lines. Resulting calculated z_0 values for each site are shown as thick vertical bars at $Q = 0 \text{ gm}^{-1}\text{s}^{-1}$. The vertical range of these bars corresponds to uncertainties in z_0 as determined by the linear fits.

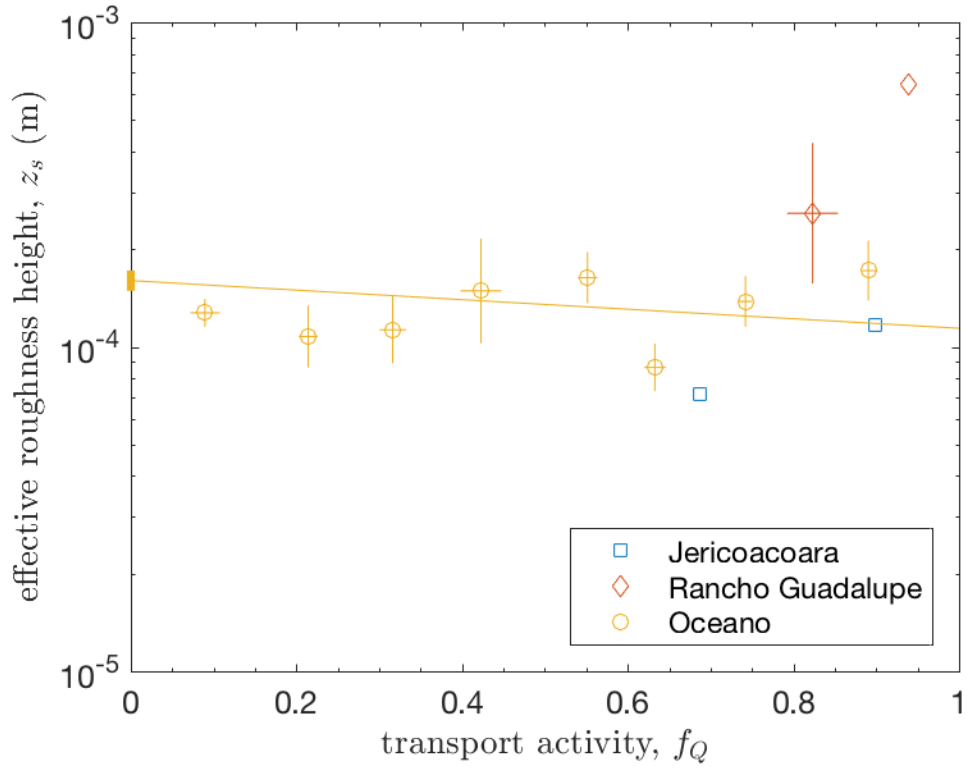


Figure S3. Comparison of effective roughness height z_s versus transport activity f_Q for intermittent transport ($0.05 < f_Q < 0.95$). Values are calculated over 30-minute intervals and combined into bins by f_Q . Ranges of 30-minute f_Q values as Jericoacoara and Rancho Guadalupe were insufficient for binning and fitting.

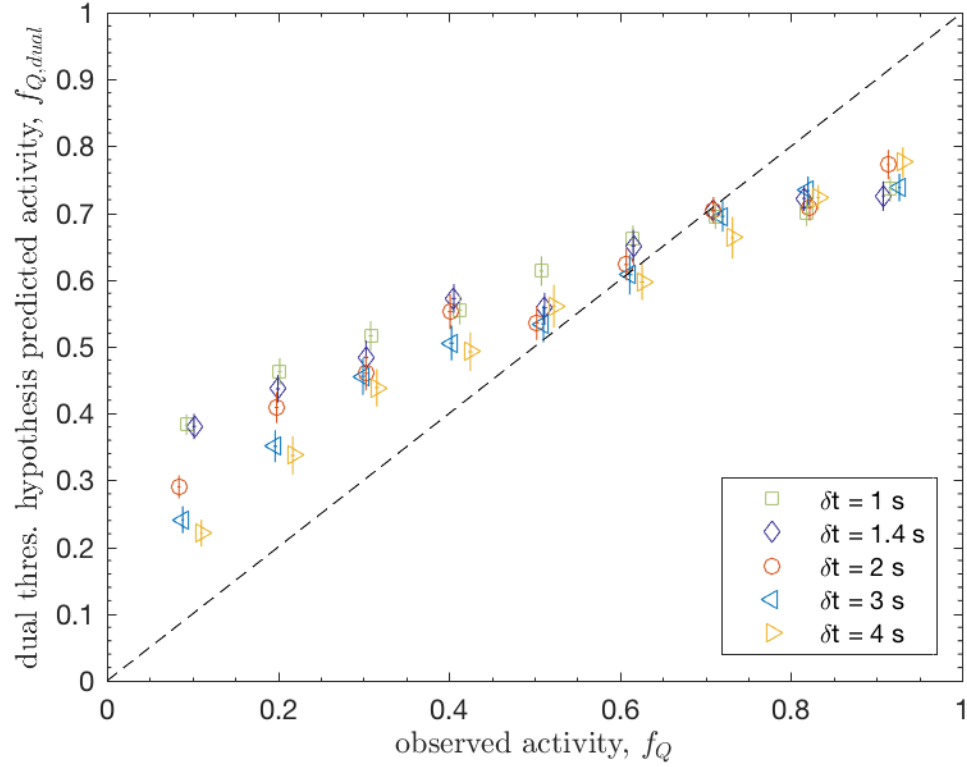


Figure S4. Comparison of observed transport activities f_Q versus those predicted for dual threshold control $f_{Q,dual}$ (Eq. 3) for five averaging intervals δt at Oceano. Analysis interval Δt was fixed here at 1 minute. Dashed line indicates agreement between observations and predictions.

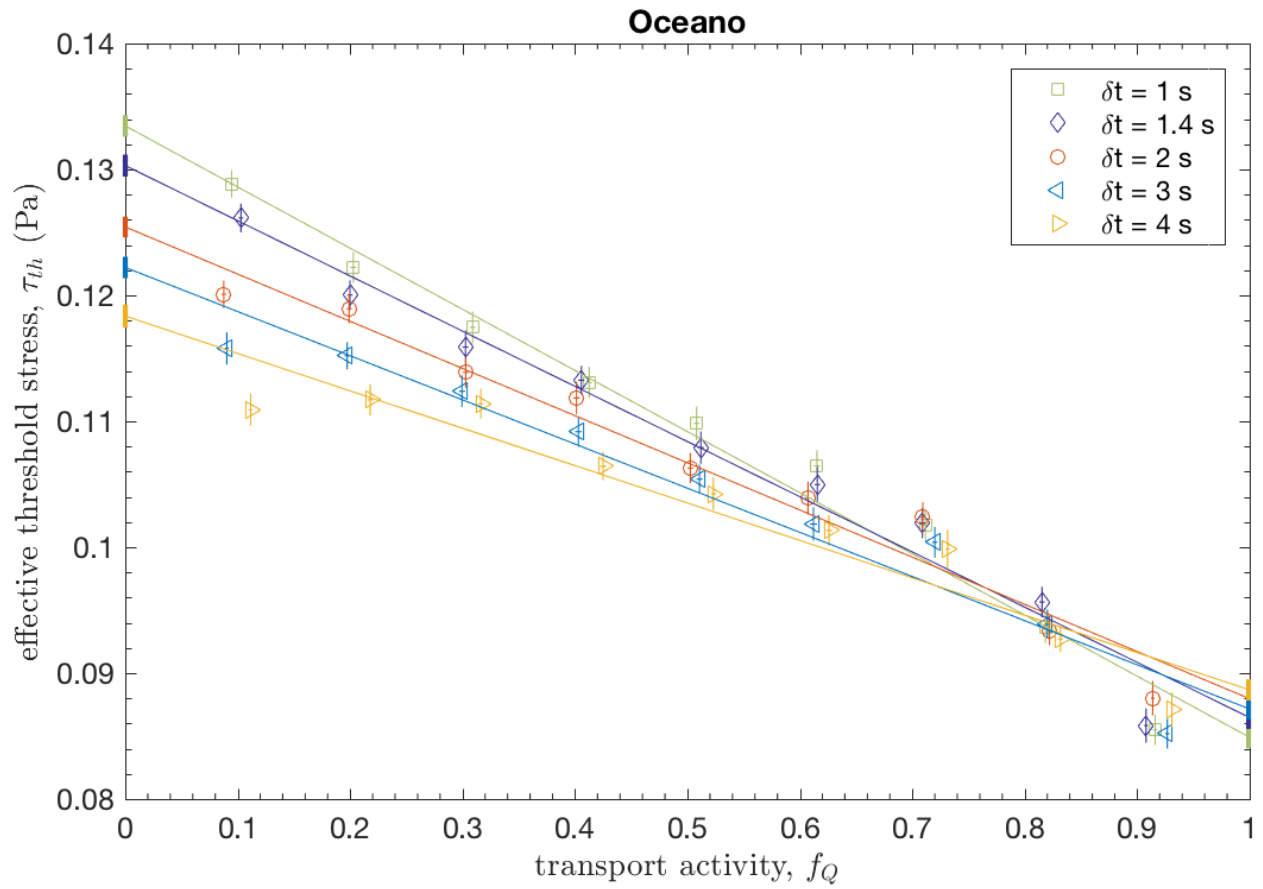


Figure S5. Comparison of effective threshold τ_{th} and transport activity f_Q for five averaging intervals δt at Oceano. Analysis interval Δt was fixed at 1 minute for this analysis. Limiting fluid and impact threshold values, indicated by vertical bars at $f_Q = 0$ and $f_Q = 1$, respectively, are given in Table S2.

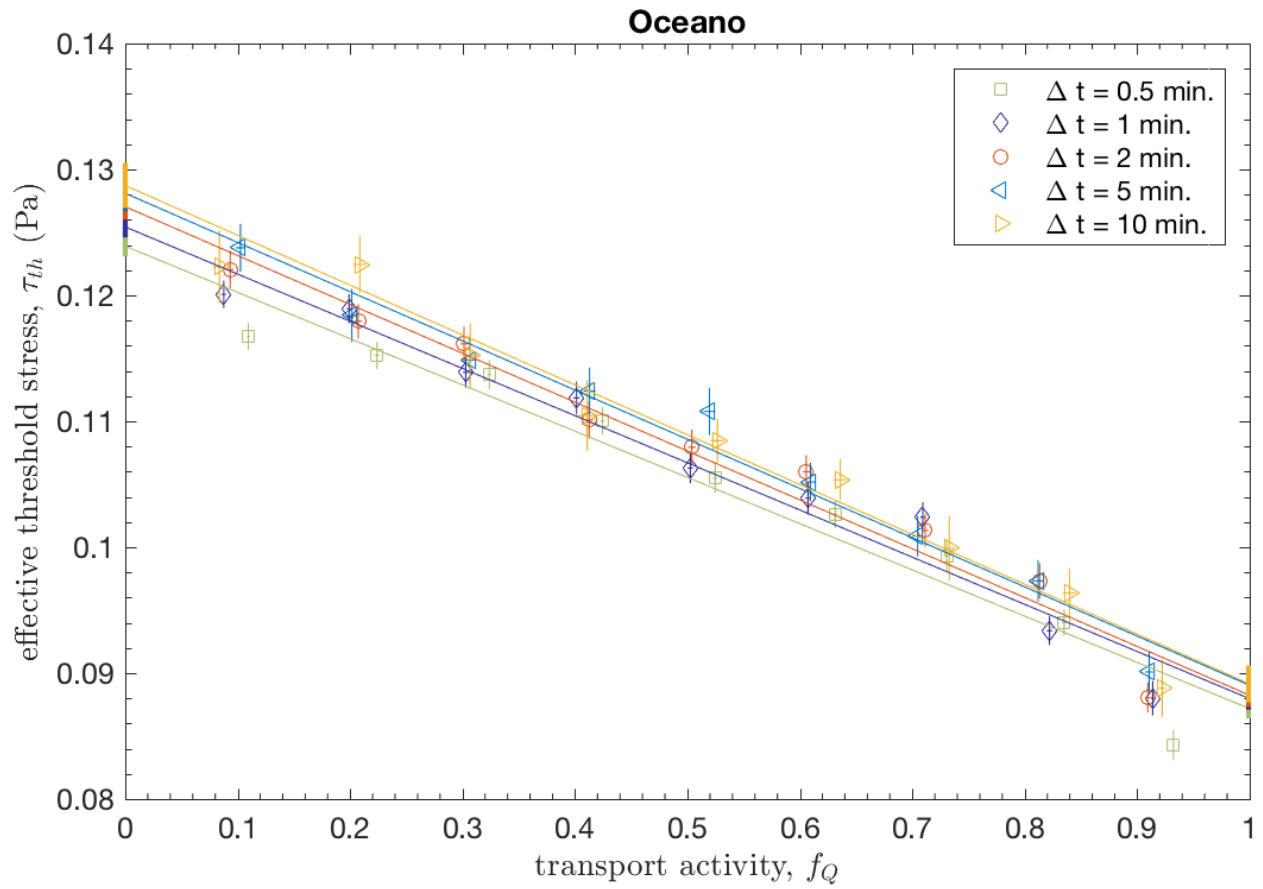


Figure S6. Comparison of effective threshold τ_{th} and transport activity f_Q for five different analysis intervals Δt at Oceano. Averaging interval δt was fixed at 2 s for this analysis. Limiting fluid and impact threshold values, indicated by vertical bars at $f_Q = 0$ and $f_Q = 1$, respectively, are given in Table S3.

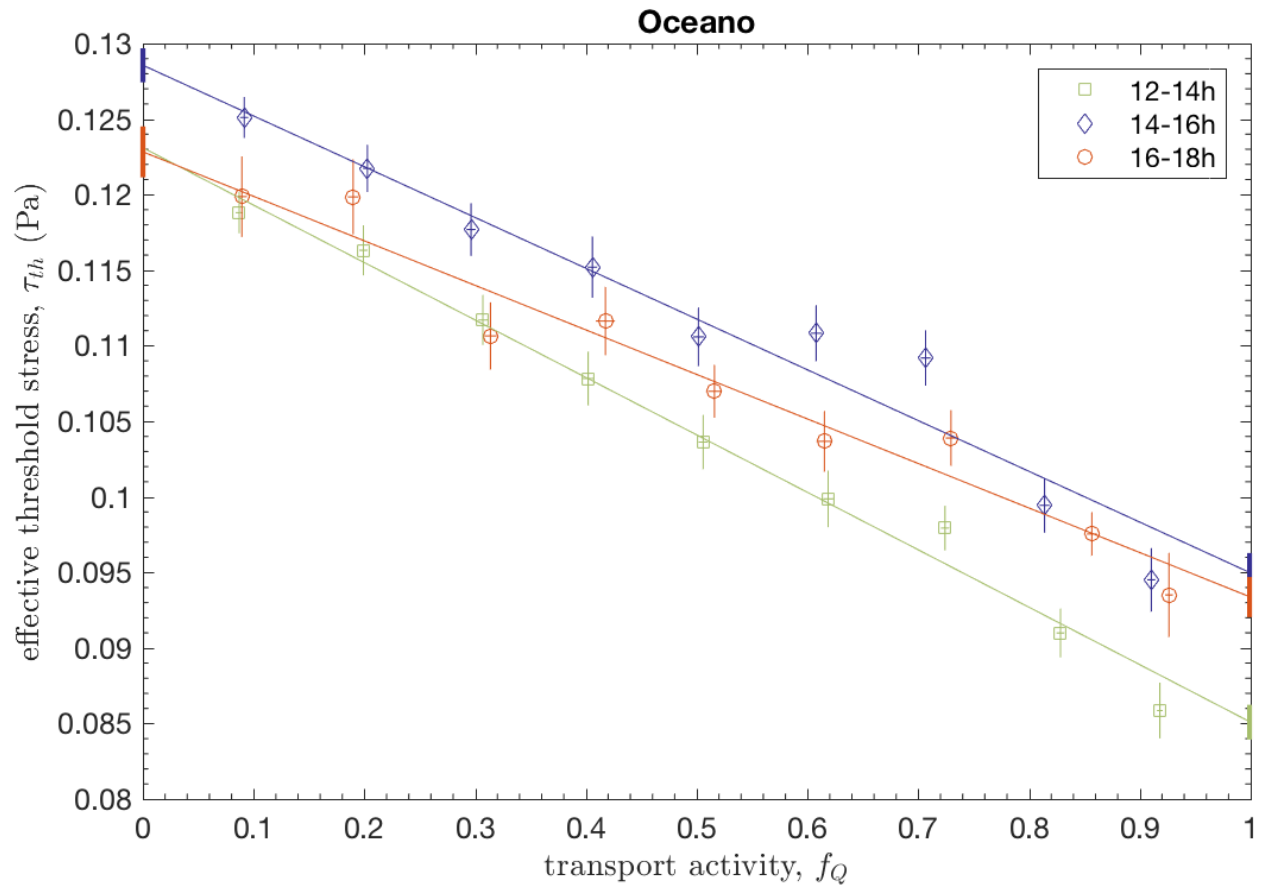


Figure S7. Comparison of effective threshold τ_{th} and transport activity f_Q for three different time periods for the diurnal cycle at Oceano. Limiting fluid and impact threshold values, indicated by vertical bars at $f_Q = 0$ and $f_Q = 1$, respectively, are given in Table S4.

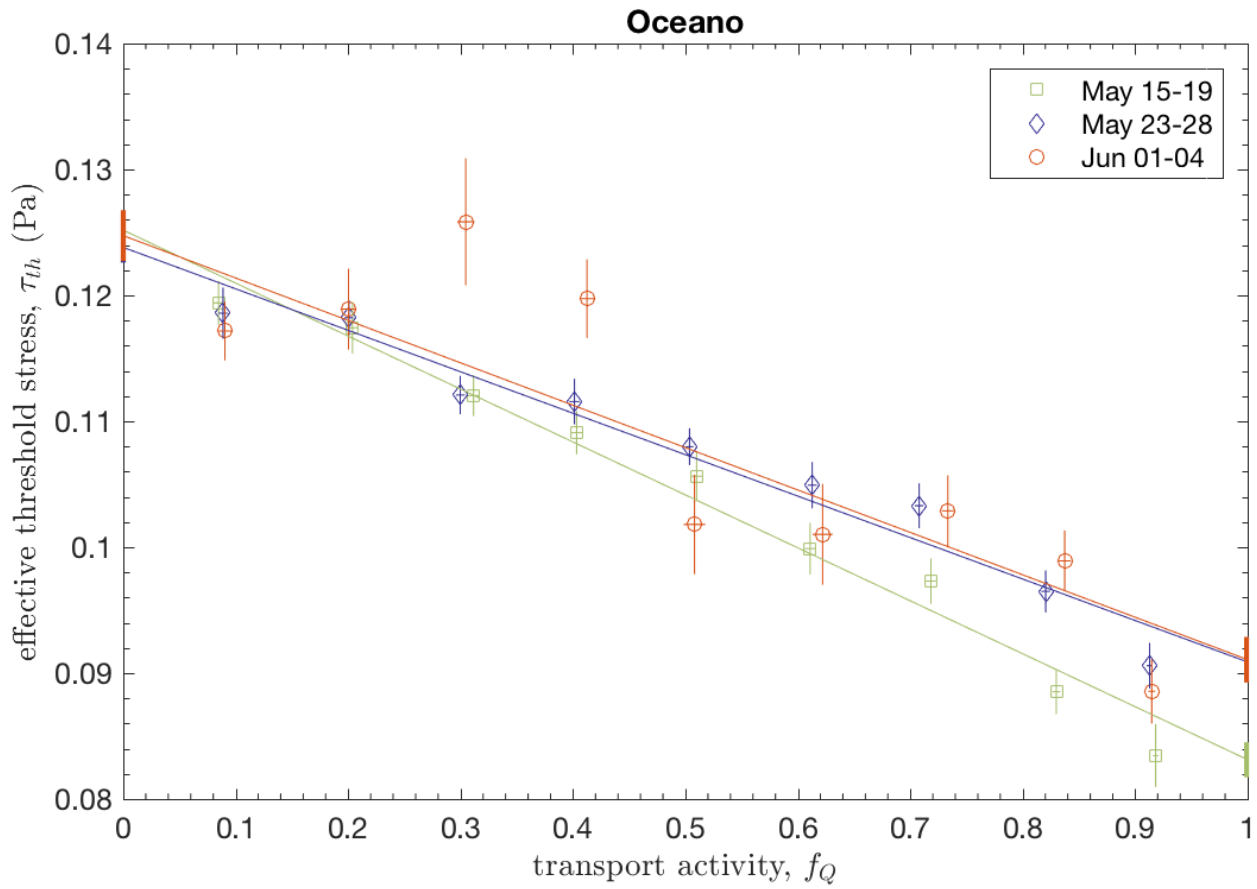


Figure S8. Comparison of effective threshold τ_{th} and transport activity f_Q for three segments of the deployment at Oceano, for which median surface grain diameter was respectively $d_{50} = 0.35$ mm, 0.42 mm, and 0.42 mm. Limiting fluid and impact threshold values, indicated by vertical bars at $f_Q = 0$ and $f_Q = 1$, respectively, are given in Table S5.

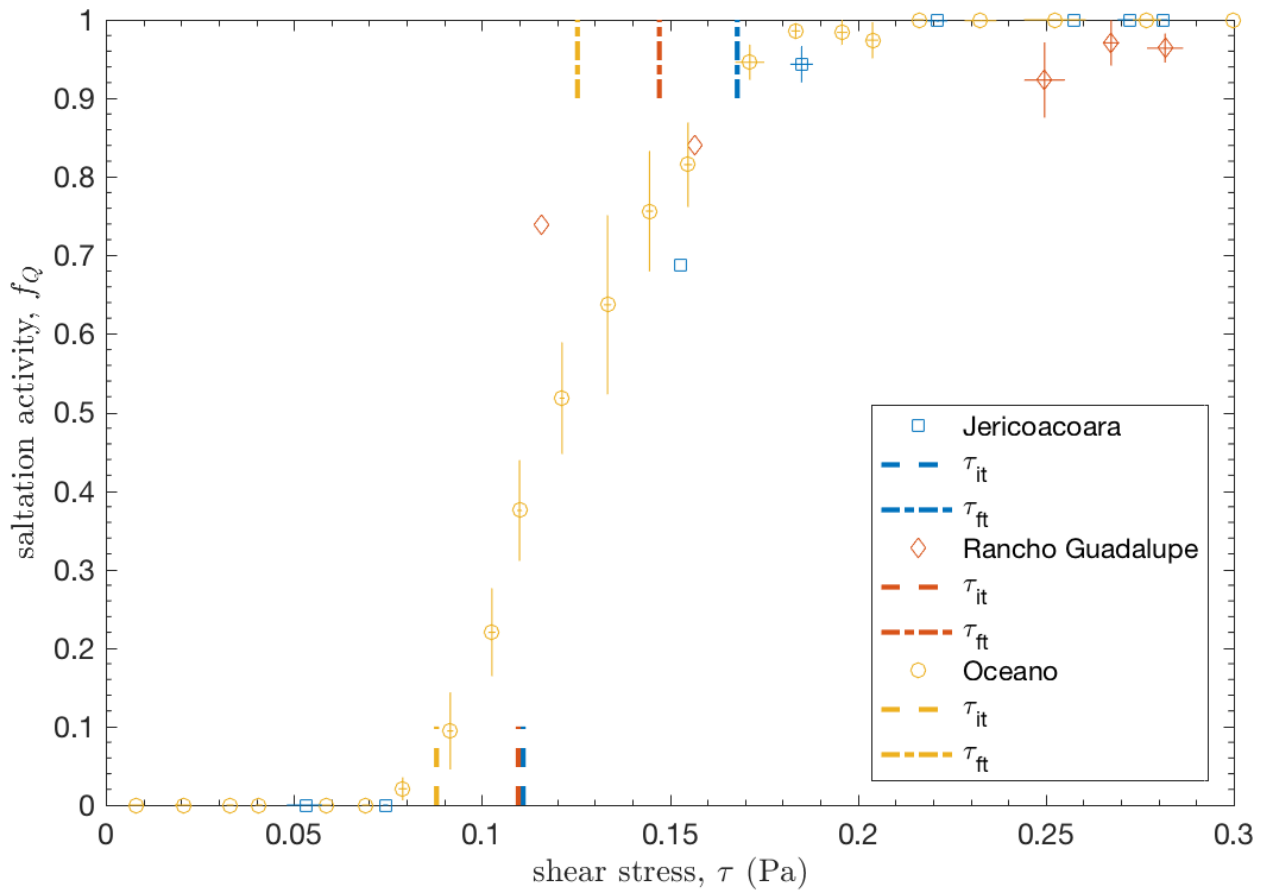


Figure S9. Saltation activity f_Q versus Reynolds shear stress τ . Values are computed over 30-minute intervals and combined into bins by range of τ . Error bars indicate standard error for each bin. Some values of $\tau > 0.3$, for which $f_Q = 1$, are not shown for clarity of the figure. Dashed lines indicate impact threshold τ_{it} and fluid threshold τ_{ft} at each site from Fig. 3.

Table S1. Threshold values for primary analysis with $\delta t = 2\text{s}$ averaging interval and $\Delta t = 1\text{ minute}$ analysis interval. Median grain diameter of surface particles at each site is also included for reference.

Site	Median grain diameter, d_{50} (mm)	Fluid threshold stress, τ_{ft} (Pa)	Impact threshold stress, τ_{it} (Pa)	Threshold ratio, $u_{*,it}/u_{*,ft}$	Threshold from flux-law fit, $\tau_{th,flux}$ (Pa)
Jericoacoara	0.526 ± 0.037	0.168 ± 0.004	0.111 ± 0.002	0.813 ± 0.018	0.135 ± 0.015
Rancho Guadalupe	0.533 ± 0.026	0.147 ± 0.006	0.110 ± 0.002	0.863 ± 0.027	0.110 ± 0.021
Oceano	0.398 ± 0.070	0.125 ± 0.001	0.088 ± 0.001	0.837 ± 0.007	0.094 ± 0.006

Table S2. Best fit values for averaging interval δt sensitivity analysis at Oceano shown in Fig. S5. Uncertainties correspond to linear fitting uncertainty, which accounts for uncertainty in individual data points used for fitting.

Averaging interval, δt (s)	Fluid threshold, τ_{ft} (Pa)	Impact threshold, τ_{it} (Pa)	Threshold ratio, $u_{*,it}/u_{*,ft}$
1	0.133 \pm 0.001	0.085 \pm 0.001	0.798 \pm 0.008
1.4	0.130 \pm 0.001	0.086 \pm 0.001	0.815 \pm 0.008
2	0.125 \pm 0.001	0.088 \pm 0.001	0.837 \pm 0.007
3	0.122 \pm 0.001	0.087 \pm 0.001	0.844 \pm 0.007
4	0.118 \pm 0.001	0.089 \pm 0.001	0.866 \pm 0.007

Table S3. Best fit values for the sensitivity analysis of the analysis interval Δt , shown in Fig. S6 for Oceano.

Analysis interval, Δt (minutes)	Fluid threshold, τ_{ft} (Pa)	Impact threshold, τ_{it} (Pa)	Threshold ratio, $u_{*,it}/u_{*,ft}$
1	0.124 ± 0.001	0.087 ± 0.001	0.839 ± 0.007
1.4	0.125 ± 0.001	0.088 ± 0.001	0.837 ± 0.007
2	0.127 ± 0.001	0.088 ± 0.001	0.833 ± 0.008
3	0.128 ± 0.001	0.089 ± 0.001	0.834 ± 0.010
4	0.129 ± 0.002	0.089 ± 0.001	0.832 ± 0.013

Table S4. Best fit values for diurnal cycle sensitivity analysis shown in Fig. S7 for Oceano.

Diurnal time interval	Fluid threshold, τ_{ft} (Pa)	Impact threshold, τ_{it} (Pa)	Threshold ratio, $u_{*,it}/u_{*,ft}$
12-14h	0.123 \pm 0.001	0.085 \pm 0.001	0.831 \pm 0.010
14-16h	0.129 \pm 0.001	0.095 \pm 0.001	0.859 \pm 0.010
16-18h	0.123 \pm 0.002	0.093 \pm 0.001	0.872 \pm 0.011

Table S5. Best fit values for date interval sensitivity analysis shown in Fig. S8 for Oceano. Median surface grain diameters d_{50} are also provided for these date intervals.

Date interval	Median grain diameter, d_{50}	Fluid threshold, τ_{ft} (Pa)	Impact threshold, τ_{it} (Pa)	Threshold ratio, $u_{*,it}/u_{*,ft}$
May 15-19	0.346 ± 0.053	0.125 ± 0.001	0.083 ± 0.001	0.815 ± 0.012
May 23-28	0.417 ± 0.056	0.124 ± 0.001	0.091 ± 0.001	0.857 ± 0.010
June 1-4	0.415 ± 0.074	0.125 ± 0.002	0.091 ± 0.002	0.854 ± 0.015

Dataset S1: Activity and threshold values

A spreadsheet containing data described in this paper may be accessed through the Zenodo data repository at <http://doi.org/10.5281/zenodo.321417>. These data are for the primary analysis presented in the main text with averaging interval $\delta t = 2$ second for all $\Delta t = 1$ minute analysis intervals at each field site. The spreadsheet contains the following fields:

- Date of analysis interval (“Date”).
- Start time of analysis interval (“StartTime”).
- End time of analysis interval (“EndTime”).
- Calculated transport activity f_Q (“f_Q”).
- Calculated effective threshold wind speed u_{th} (“u_th”) in m/s. This value is undefined (“NaN”) for intervals with $f_Q = 0$ or $f_Q = 1$.
- Eq. 1 predicted transport activity $f_{Q,ft}$ (“f_Q_ft”).
- Eq. 2 predicted transport activity $f_{Q,it}$ (“f_Q_it”).
- Eq. 3 predicted transport activity $f_{Q,dual}$ (“f_Q_dual”).
- Stability parameter z/L (“z/L”) obtained from wind-speed fluctuations in corresponding 30-minute time interval. This value is sometimes undefined (“NaN”) for intervals of very weak wind.
- Wind direction θ (“theta”) in degrees. Value is relative to dominant wind direction at site.

The field measurements from which these values were calculated are described in *Martin et al.* [2017].